

Electrical switching of a *p*-wave magnet

<https://doi.org/10.1038/s41586-025-09034-7>

Received: 3 September 2024

Accepted: 16 April 2025

Published online: 28 May 2025

 Check for updates

Qian Song^{1,2}, Srdjan Stavrić^{3,4}, Paolo Barone⁵, Andrea Droghetti^{3,6}, Daniil S. Antonenko⁷, Jörn W. F. Venderbos⁸, Connor A. Occhialini¹, Batyr Ilyas¹, Emre Ergeçen¹, Nuh Gedik¹, Sang-Wook Cheong⁹, Rafael M. Fernandes^{10,11}, Silvia Picozzi^{3,12} & Riccardo Comin¹

Magnetic states with zero magnetization but non-relativistic spin splitting are outstanding candidates for the next generation of spintronic devices. Their electronvolt (eV)-scale spin splitting, ultrafast spin dynamics and nearly vanishing stray fields make them particularly promising for several applications^{1,2}. A variety of such magnetic states with non-trivial spin textures have been identified recently, including even-parity *d*-wave, *g*-wave or *i*-wave altermagnets and odd-parity *p*-wave magnets^{3–7}. Achieving voltage-based control of the non-uniform spin polarization of these magnetic states is of great interest for realizing energy-efficient and compact devices for information storage and processing^{8,9}. Spin-spiral type II multiferroics are optimal candidates for such voltage-based control, as they exhibit an inversion-symmetry-breaking magnetic order that directly induces ferroelectric polarization, allowing for symmetry-protected cross-control between spin chirality and polar order^{10–14}. Here we combine photocurrent measurements, first-principles calculations and group-theory analysis to provide direct evidence that the spin polarization of the spin-spiral type II multiferroic NiI₂ exhibits odd-parity character connected to the spiral chirality. The symmetry-protected coupling between chirality and polar order enables electrical control of a primarily non-relativistic spin polarization. Our findings represent an observation of *p*-wave magnetism in a spin-spiral type II multiferroic, which may lead to the development of voltage-based switching of non-relativistic spin polarization in compensated magnets.

Recent advances in spin-group classification^{3,4,15} have led to the prediction and subsequent observation of collinear altermagnets^{6,7}, a new class of magnets with fully compensated magnetic moments but exhibiting strong non-relativistic spin splitting, that is, spin splitting that persists even without spin-orbit coupling (SOC)^{16–18}. Similarly, non-collinear magnetic states can also exhibit spin splitting^{19–22}, and recent spin-group analysis has shown that certain non-collinear compensated magnetic configurations can sustain sizeable odd-parity spin polarization even in the absence of SOC^{5,23–25} (Extended Data Fig. 1). Here spin polarization refers to the expectation value of the spin angular momentum operator over Bloch states in momentum space. A key feature of odd-parity magnets is that the inversion operation reverses the spin polarization, suggesting the possibility of controlling the primarily non-relativistic spin texture electrically when SOC is accounted for.

Non-collinear spin-spiral (type II) multiferroics exhibit inversion-symmetry-breaking magnetic order characterized by spin chirality (the handedness of the helix), which can induce improper ferroelectric polarization through SOC^{26,27}, allowing for electrical control of compensated magnetic states^{28–31}. Although previous studies have focused on the interplay between spin chirality and ferroelectricity in

spin-spiral multiferroics, here we demonstrate that predominantly non-relativistic spin polarization is also present and can be controlled electrically.

Symmetries of the spin helix in NiI₂

The van der Waals (vdW) material NiI₂ has been identified as a spin-spiral type II multiferroic^{32–34}. NiI₂ takes up the rhombohedral $R\bar{3}m$ structure at room temperature, which comprises triangular lattices of Ni²⁺ ions (with spin $S=1$) stacked along the *c* axis (Fig. 1a). The two-dimensional triangular lattice geometrically frustrates the intralayer magnetic exchange interactions between Ni spins^{35–38}. This leads to a sequence of magnetic phase transitions, first to an antiferromagnetic state at $T_{N,1} \approx 75$ K and then to a helimagnetic ground state below $T_{N,2} \approx 59.5$ K (see Extended Data Fig. 2 for structure and magnetometry characterization). The latter is characterized by an incommensurate, proper-screw spin helix with propagation vector $\mathbf{Q} = (0.138, 0, 1.457)$ reciprocal lattice units (r.l.u.). In terms of the real-space coordinates $x \parallel [100]$, $y \parallel [120]$ and $z \parallel [001]$, \mathbf{Q} lies on the *y*–*z* plane. The helix is tilted from the *c* axis by about 35°, with the spin-spiral plane suggested to be nearly normal to \mathbf{Q} (refs. 39,40). As a result of SOC, which locks the

¹Department of Physics, Massachusetts Institute of Technology, Cambridge, MA, USA. ²Department of Materials Science and Engineering, Massachusetts Institute of Technology, Cambridge, MA, USA. ³Consiglio Nazionale delle Ricerche CNR-SPIN, c/o Università degli Studi 'G. D'Annunzio', Chieti, Italy. ⁴Vinča Institute of Nuclear Sciences – National Institute of the Republic of Serbia, University of Belgrade, Belgrade, Serbia. ⁵Consiglio Nazionale delle Ricerche CNR-SPIN, Area della Ricerca di Tor Vergata, Rome, Italy. ⁶Department of Molecular Sciences and Nanosystems, Ca' Foscari University of Venice, Venice, Italy. ⁷Department of Physics, Yale University, New Haven, CT, USA. ⁸Department of Physics, Drexel University, Philadelphia, PA, USA. ⁹Keck Center for Quantum Magnetism and Department of Physics and Astronomy, Rutgers University, Piscataway, NJ, USA. ¹⁰Department of Physics, The Grainger College of Engineering, University of Illinois Urbana-Champaign, Urbana, IL, USA. ¹¹Anthony J. Leggett Institute for Condensed Matter Theory, The Grainger College of Engineering, University of Illinois Urbana-Champaign, Urbana, IL, USA.

¹²Department of Materials Science, University of Milano-Bicocca, Milan, Italy. [✉]e-mail: qiansong@mit.edu; rafael@illinois.edu; rcomin@mit.edu

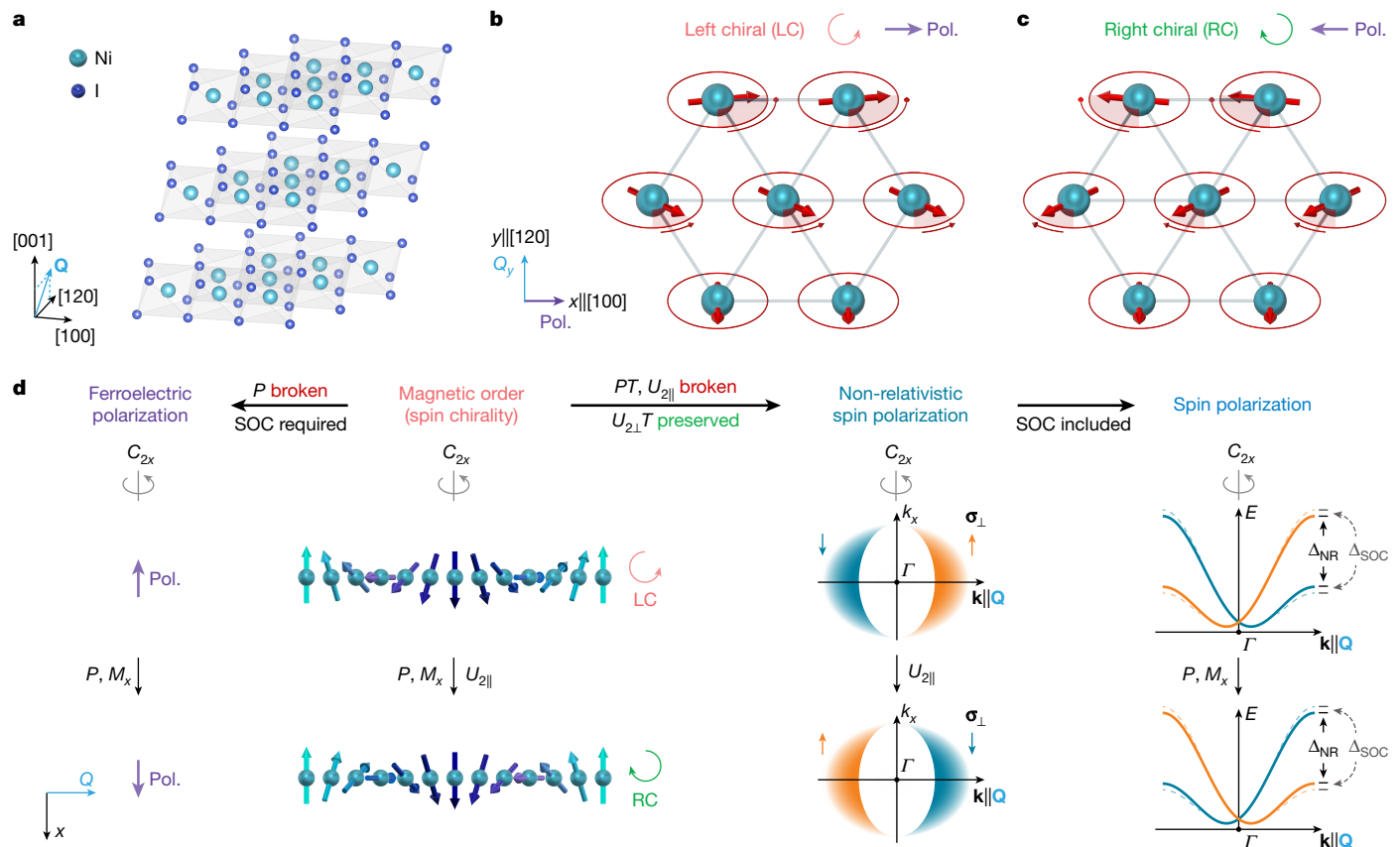


Fig. 1 | Symmetry-protected magnetoelectric coupling in type II multiferroic NiI_2 . **a**, Lattice structure of NiI_2 below $T_{\text{N},2} = 59.5$ K, with spin helix propagation vector $\mathbf{Q} = (0.138, 0, 1.457)$ reciprocal lattice units (r.l.u.), lying in the $[120]/[001]$ plane. **b,c**, Magnetoelectric coupling between spin chirality and the spin-induced ferroelectric polarization (Pol.). Q_y is the in-plane component of the spin helix propagation vector. The polar axis [100] is perpendicular to Q_y . **d**, Symmetry-protected coupling between ferroelectric and (non-relativistic) spin polarization in NiI_2 . On the one hand, the spin chirality of the chiral magnetic order breaks inversion symmetry, induces ferroelectric polarization and couples to it. On the other hand, the chiral magnetic order breaks PT and $U_{2\parallel}$ symmetries, giving rise

to odd-parity non-relativistic spin polarization σ_\perp , protected by $U_{2\perp}T$, $U_{2\parallel}$ and $U_{2\perp}$ represent twofold spin rotation with axes parallel and perpendicular to the spin-spiral plane, respectively. σ_\perp represents spin perpendicular to the spin-spiral plane. This non-relativistic effect promotes a substantial spin splitting (Δ_{NR}), much larger than that arising from SOC (Δ_{SOC}). The symmetry operations that switch ferroelectric polarization will also switch (non-relativistic) spin polarization, allowing for C_{2x} -symmetry-protected electrical control of (non-relativistic) spin polarization. The solid lines represent the schematic of non-relativistic spin-polarized bands and the dashed lines represent those that include SOC.

spins to the lattice and implies that spin and spatial coordinates transform jointly, the helical magnetic order in NiI_2 breaks nearly all rotational and mirror symmetries of the host lattice and only retains a single twofold (C_2) axis perpendicular to the in-plane projection of the propagation vector \mathbf{Q} (ref. 41) (see Extended Data Fig. 3 and Supplementary Information 1 for detailed symmetry analysis). Consequently, the helimagnetic transition is concomitant with the appearance of an in-plane ferroelectric polarization along the unique C_2 axis³², establishing NiI_2 as a spin-spiral type II multiferroic. Indeed, a pair of non-collinear spins generates, through a spin-current mechanism²⁶, an electric dipole with the general form $\mathbf{P}_{ij} = \mathbf{M}_{ij} \cdot (\vec{S}_i \times \vec{S}_j)$. Here i and j are lattice sites, an arrow denotes an axial vector and boldface denotes a polar vector/tensor. \mathbf{M}_{ij} is the antisymmetric part of a polar rank 3 tensor that describes the coupling between two non-collinear spins and electric dipole⁴². The sign of $\vec{S}_i \times \vec{S}_j$ denotes the (vector) spin chirality. In the aforementioned spin spiral, summing over all bonds gives a total polarization that is proportional to the total spin chirality (see Supplementary Information Section 2 for a detailed symmetry analysis of \mathbf{M}_{ij} and the resulting macroscopic polarization). It is important to emphasize that no symmetry operation exists that solely reverses either spin chirality or ferroelectric polarization while leaving the other unchanged, thereby establishing a symmetry-protected magnetoelectric coupling with record strength⁴³ in NiI_2 , as shown in Fig. 1b,c.

This strong coupling enables reliable electrical control of spin chirality through switching of the ferroelectric polarization, as observed in many other spin-spiral multiferroics^{29–31}.

A comprehensive analysis of the symmetry properties of a spin helix is essential for understanding the link between ferroelectric polarization and momentum-space spin polarization. The latter is quantified by the spin expectation value at momentum \mathbf{k} and band n , $\langle \sigma \rangle = \frac{1}{2} \langle \psi_n(\mathbf{k}) | \sigma | \psi_n(\mathbf{k}) \rangle$, in which $\psi_n(\mathbf{k})$ is the Bloch wave function and σ is the spin operator. Figure 1d illustrates how the symmetry properties of the spiral anchor the relationship between ferroelectric polarization, spin chirality and spin polarization in NiI_2 . As depicted in Fig. 1d, the spiral in NiI_2 has a twofold rotational symmetry axis along x (C_{2x}), which specifies the unique axis of ferroelectric polarization (purple arrows) and the spin polarization nodal line ($k_y = k_z = 0$). As a result, when inversion (P) or reflection with respect to the $y-z$ plane (M_x) switches the spin chirality (orange and green arrows), the charge and spin polarizations switch as well, thereby establishing symmetry-protected coupling between these three quantities. Notably, for these symmetry operations to act on both real space and spin space, we need to invoke the existence of SOC. To establish a connection between these three quantities, we may be tempted to invoke a Rashba-like mechanism, by which a ferroelectric polarization generates an odd-parity spin polarization of the form $\langle \sigma_i(\mathbf{k}) \rangle = -\langle \sigma_i(-\mathbf{k}) \rangle$. Although such a contribution indeed exists,

the crucial point is that here the odd-parity spin polarization arises even in the absence of SOC^{5,23}.

To demonstrate this, we consider spin-group symmetry operations with rotations in spin space independent from rotations in real space. Twofold spin-space rotations about the n axis are denoted as U_{2n} , distinct from magnetic-space rotations C_{2n} . As shown in the middle two panels of Fig. 1d, the spin helix breaks PT symmetry but remains invariant under $U_{2\perp}T$, in which $U_{2\perp}$ (twofold spin rotation perpendicular to the spiral plane) compensates time-reversal T (ref. 5). By contrast, a twofold spin rotation parallel to the spiral plane ($U_{2\parallel}$) reverses spin chirality (Supplementary Information Section 1). These symmetries enforce an odd-parity spin polarization with p -wave-like symmetry, $\langle \sigma_\perp(\mathbf{k}) \rangle = -\langle \sigma_\perp(-\mathbf{k}) \rangle$, in which $\mathbf{k} \parallel \mathbf{Q}$, as illustrated in the non-relativistic spin polarization panel, leading to a non-relativistic spin splitting Δ_{NR} . More symmetries may further constrain the properties of odd-parity spin polarization. For instance, an even-period commensurate spiral retains $T\tau$ symmetry (in which τ is a real-space translation), enforcing Kramer's degeneracy^{5,23–25}. In the absence of SOC, whereas $T\tau$ symmetry enforces spin degeneracy in a collinear antiferromagnet, it protects the odd-parity spin polarization in non-collinear non-centrosymmetric compensated magnets (Supplementary Fig. 3). Given that odd-parity spin polarization persists without SOC and is linked to spin chirality through spin-group symmetries, we now examine its behaviour with SOC. As we will show in our density functional theory (DFT) results, the magnitude of the spin splitting is only weakly affected by the SOC (Δ_{SOC}). The primary role of SOC is to enable direct coupling between ferroelectric polarization and predominantly non-relativistic spin polarization, enabling electrical control and examination of spin polarization.

The odd-parity spin splitting in spiral magnets can also be understood through a simple model in which itinerant electrons couple to winding magnetic moments through a Kondo-like interaction^{44–48}. Recently linked to kinetomagnetism^{49–53}, this model shows that, in a one-dimensional spin helix, electronic bands experience an odd-parity Zeeman field⁴⁶ $h_\perp(\mathbf{k}) = (\mathbf{k} \cdot \mathbf{Q})/2m$ polarized perpendicular to the spiral plane (Extended Data Fig. 4a,b). This expression explicitly connects spin splitting and chirality ($h_\perp \sigma_\perp \propto k_\perp \sigma_\perp$), while revealing that spin splitting remains unaffected by the Kondo coupling, instead scaling with effective mass and wavevector magnitude Q , suggesting a substantial spin splitting for short-period spin helices (Supplementary Information Section 3).

DFT calculations for the spin helix

As discussed above, symmetry considerations indicate that NiI_2 exhibits odd-parity spin splitting of predominantly non-relativistic character. Although in experiments it is impossible to distinguish the two contributions (relativistic and non-relativistic), DFT offers an ideal framework to probe this issue. Therefore, we use non-collinear DFT to analyse the momentum-space spin polarization in the helimagnetic state of NiI_2 (see Methods for computational details). Simulating the realistic incommensurate helimagnetism of bulk NiI_2 is computationally challenging, requiring large simulation cells and thus making the analysis of band structure and its spin polarization unnecessarily convoluted. Instead, we consider an isolated NiI_2 monolayer, making use of its vdW nature and weak interlayer coupling (Extended Data Fig. 5). Within a single layer, the bulk helimagnetic state can be seen as a spiral propagating along the in-plane component of the propagation vector, with spins rotating in a plane that contains the twofold rotation axis (C_{2x}) perpendicular to the spiral wavevector. In our monolayer model, therefore, the spiral can be decomposed in a proper-screw helical part, with the spin-spiral plane perpendicular to the in-plane propagation vector, and in a cycloidal component with spins rotating within the layer. Without loss of generality, we take the propagation vector parallel to the $y\parallel[120]$ direction and the spin-spiral plane perpendicular to

$z\parallel[001]$, that is, a cycloidal-type spin spiral, as depicted in Extended Data Fig. 6. From a symmetry perspective, this cycloidal-type spiral is equivalent to the proper-screw spin spiral, as—in both cases—the ferroelectric polarization can only develop parallel to the twofold rotation axis (Supplementary Information Sections 2 and 4), whereas the (non-relativistic) spin polarization is expected to develop perpendicular to the spin-spiral plane.

Figure 2a shows the momentum-dependent expectation value $\langle \sigma_z(\mathbf{k}) \rangle$ for a period 3 left-handed helix without SOC. The expectation value vanishes along $X-\Gamma-X'$ but is non-zero and antisymmetric along $Y-\Gamma-Y'$ for both conduction and valence bands. Here $X-\Gamma-X'$ is aligned to the ferroelectric polarization ($\text{Pol.} \parallel [100]$), whereas $Y-\Gamma-Y'$ is along the in-plane spin helix propagation axis ($Q_y \parallel [120]$). Thus, the spin polarization is symmetric along the ferroelectric polarization direction but antisymmetric along Q_y , protected by local C_{2x} symmetry. Also, both $\langle \sigma_x(\mathbf{k}) \rangle$ and $\langle \sigma_y(\mathbf{k}) \rangle$ vanish in the absence of SOC (Extended Data Fig. 5 and Supplementary Fig. 2), supporting a spin polarization axis orthogonal to the spiral plane. This is further confirmed by rotating the spiral plane (Extended Data Fig. 4c,d), for which a proper-screw spiral in the $x-z$ plane shows a spin polarization axis parallel to y . Figure 2b presents the non-relativistic spin polarization of the left chiral helix at constant energy $E = E_{\text{VBM}} - 0.95$ eV. Notably, as the spin chirality switches, the non-relativistic spin polarization also reverses, as shown in Fig. 2c, supporting the coupling between the odd-parity non-relativistic spin polarization and spin chirality in NiI_2 . The inclusion of SOC (Fig. 2d) leads to further spin splittings but does not substantially change the magnitude at the Y point, highlighting the dominance of the non-relativistic contribution. Although details of the $\langle \sigma_z(\mathbf{k}) \rangle$ spin polarization are affected by SOC, thus depending on the spiral pitch and rotation plane, its odd-parity character and connection with spin chirality are consistently preserved, as seen in Fig. 2e,f.

Electrical switching of polarization in NiI_2

On the basis of the above theoretical analysis, we expect that the spin chirality in NiI_2 can be reversed by switching the spin-induced ferroelectric polarization. Figure 3a shows the ferroelectric polarization along the principal axis [100], measured using the pyroelectric current method in a bulk NiI_2 sample. An in-plane poling electric field of $E = \pm 20$ kV m⁻¹ was applied during cooling and removed before the current measurement in the warming process. A sharp peak in the pyroelectric current near 59.5 K reflects the depolarization at the multiferroic transition temperature (shaded region). With the poling electric field reversed, the pyroelectric current also changes sign, demonstrating the electrical switching of spin-induced ferroelectric order. A polarization of around $42 \mu\text{C m}^{-2}$ was obtained on time integration of the pyroelectric current (solid line). For micron-scale NiI_2 samples, measurements of the electrical polarization become challenging, as the pyroelectric current scales with the sample dimension (details in Extended Data Fig. 7). Therefore, a local probe of polar order in a single spin helix domain region, which has typical lateral dimension of 10 μm (ref. 33), is essential to investigate the p -wave spin polarization, as different spin textures are realized in different domains, governed by local C_2 symmetries.

In this study, we used zero-bias photocurrent as a sensitive local probe of polar order. A 20-nm-thick NiI_2 flake was transferred with principal axis [100] aligned between two gold electrodes, as shown in Fig. 3b (see optical image in Extended Data Fig. 7d). A poling electric field of $E = \pm 2$ MV m⁻¹ was applied to the NiI_2 flake in the cooling process and the photocurrent was measured using 532-nm photoexcitation at zero bias in the warming process. The bulk photovoltaic effect in the multiferroic phase of NiI_2 is because of the built-in electrical polarization, producing a finite zero-bias photocurrent^{33,54} (see Extended Data Fig. 7g–i for more details). Figure 3c shows the temperature dependence of zero-bias

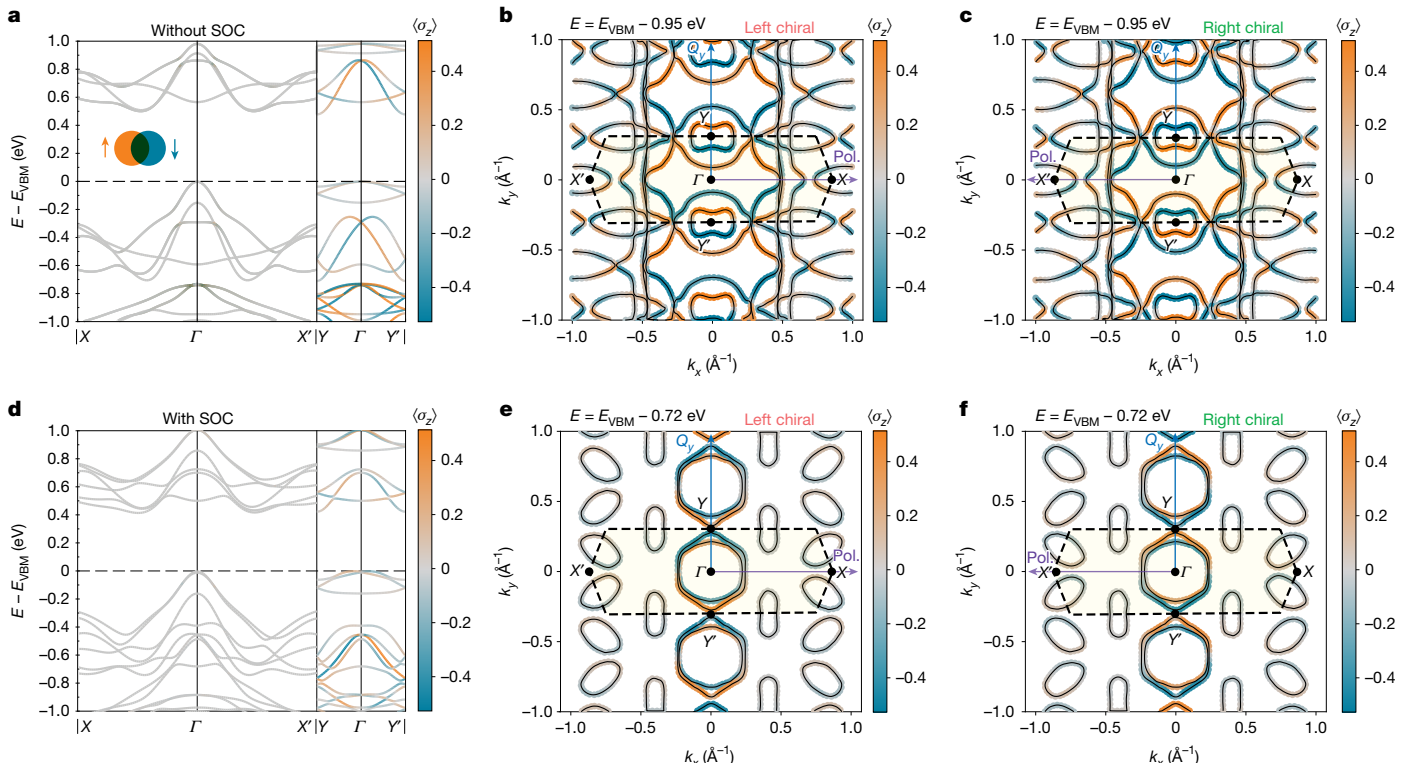


Fig. 2 | DFT study of spin polarization in NiI_2 . **a–f**, Electronic bands of the period 3 spiral in NiI_2 superimposed with the momentum-dependent $\langle \sigma_z(\mathbf{k}) \rangle$ spin expectation values calculated along the band dispersion without SOC (**a**) and with SOC (**d**). The spin-degenerate bands are coloured in grey. The ferroelectric polarization (Pol.) is along the $X-\Gamma-X'$ direction, whereas the spin helix propagates along the $Y-\Gamma-Y'$ direction. The $\langle \sigma_z(\mathbf{k}) \rangle$ expectation value vanishes along $X-\Gamma-X'$ but is non-zero and antisymmetric along $Y-\Gamma-Y'$, showing a p -wave character. This $\langle \sigma_z(\mathbf{k}) \rangle$ spin polarization is protected by the C_{2x} symmetry and persists even in the absence of SOC. $\langle \sigma_z(\mathbf{k}) \rangle$ spin polarization in

the absence of SOC for left chiral (**b**) and right chiral (**c**) at constant energy cut $E = E_{\text{VBM}} - 0.95$ eV. The spin polarization is antisymmetric along k_y and symmetric along k_x . The spin polarization reverses on switching the spin chirality. $\langle \sigma_z(\mathbf{k}) \rangle$ spin polarization with SOC for left chiral (**e**) and right chiral (**f**) at constant energy cut $E = E_{\text{VBM}} - 0.72$ eV. The odd-parity character of $\langle \sigma_z(\mathbf{k}) \rangle$ spin polarization and its coupling to spin chirality are preserved regardless of SOC. X, X', Y and Y' are the high-symmetry points at the boundary of the first Brillouin zone (area within the dashed hexagon).

photocurrent for opposite field cooling. The intensity and sign of the photocurrent reflect the net ferroelectric polarization, which vanishes above the multiferroic transition temperature. This spin-induced ferroelectric polarization can also be repeatedly switched back and forth in the multiferroic phase by applying ± 12 MV m $^{-1}$ pulsed electric field at 30 K, as shown in Fig. 3d. Complete ferroelectric hysteresis loops as a function of temperature were acquired by applying a sequence of pulsed electric fields, as shown in Fig. 3e. The coercive and saturation fields are around 5 MV m $^{-1}$ and 10 MV m $^{-1}$ at 30 K, respectively. The kinks and sharp jumps in the hysteresis loop can be ascribed to domain redistribution after applying pulsed electric field 55 , as zero-bias photocurrent only examines ferroelectric polarization in a micron-sized field of view. The coercive field is reduced as temperature is increased and the loop closes above the transition temperature (60 K). The dependence of the zero-bias photocurrent signal on temperature and electric field confirms that it is a sensitive local probe of polar order in spin-spiral type II multiferroic NiI_2 .

Odd-parity spin polarization in NiI_2

The presence of odd-parity spin splitting driven by SOC in Rashba and Weyl systems has been previously investigated using the circular photogalvanic effect (CPGE) $^{56–59}$. Because of the angular momentum of a circularly polarized pulse, the CPGE assesses optical transitions between electronic states with opposite spin angular momenta. To assess the odd-parity spin polarization in NiI_2 , it is essential to perform the CPGE measurement within a single spin helix domain to avoid signal

cancellation from several domains (see Extended Data Fig. 8a for details of single domain selection procedure). NiI_2 , with a triangular lattice, exhibits three pairs of equivalent spin helix domains 32,33 . The propagation direction of the spin helix can be identified using linear dichroism, which distinguishes in-plane \mathbf{Q} orientations through the associated breaking of threefold rotational symmetry C_{3z} (ref. 33). Spatial mapping and angular dependence of linear dichroism in our flake reveal a single domain with propagation vector Q_y along [120] (Extended Data Fig. 8b–d). Each propagation direction hosts left and right chiral domains with opposite ferroelectric polarization perpendicular to Q_y , which can be controlled through electric-field cooling (Extended Data Fig. 8f). To investigate odd-parity spin polarization using CPGE, the angular momentum of the incident light needs to have a component along the band's spin polarization axis, whereas the photocurrent detection needs to be along the direction in which the spin texture is antisymmetric. In the case of NiI_2 , we used 680-nm photoexcitation at normal incidence, as the axis perpendicular to the spin-spiral plane has a large out-of-plane spin component, and the photocurrent detection is along the Q_y direction, which—according to the symmetry analysis and DFT—is the direction along which the $\langle \sigma_z(\mathbf{k}) \rangle$ spin polarization has odd parity.

The CPGE device has two pairs of electrodes, as shown in Fig. 4g. One pair is along the ferroelectric polarization direction [100], to switch and scrutinize the ferroelectric polarization, and the other pair of electrodes is along the Q_y direction [120] to examine the odd-parity spin polarization. The incident light polarization is tuned by rotating an achromatic quarter-wave plate. The wavelength dependence of the

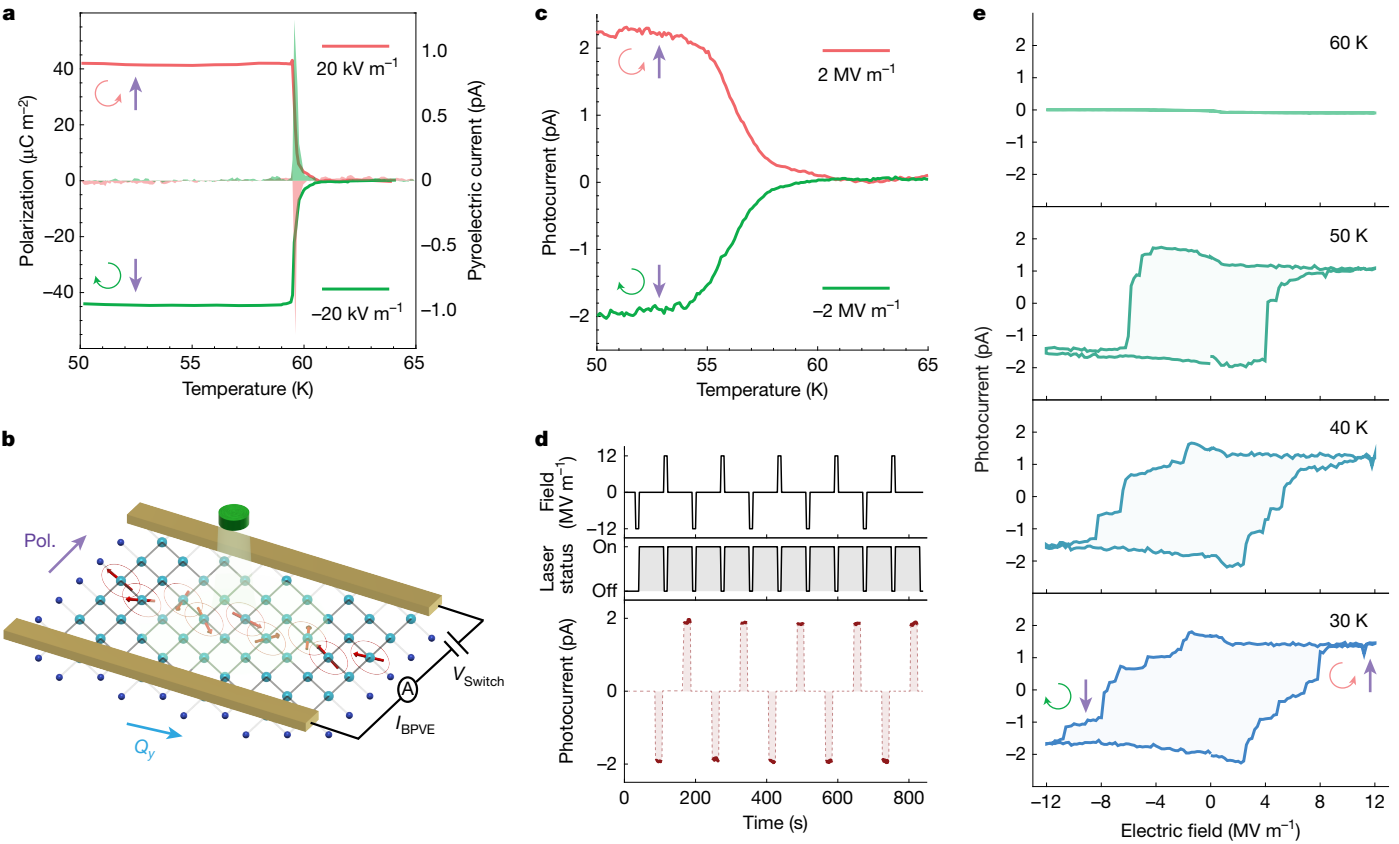


Fig. 3 | Polarization switching of NiI_2 . **a**, Pyroelectric current measured in a bulk NiI_2 sample (shaded area). The electric polarization was extracted from time integration of the pyroelectric current (solid line). **b**, Schematic of zero-bias photocurrent measurement. The electrodes are placed along the ferroelectric polarization direction. Iodine atoms on top of nickel are hidden for clarity. Ferroelectric polarization and in-plane spin helix propagation directions are denoted as purple arrow Pol. and blue arrow Q_y , respectively; photocurrent generated from the bulk photovoltaic effect is labelled as I_{BPVE} ; the voltage

required to switch the ferroelectric polarization is represented as V_{Switch} . **c**, Temperature-dependent zero-bias photocurrent measurement in a 20-nm-thick NiI_2 flake. **d**, Repeatable polarization switching by applying $\pm 12 \text{ MV m}^{-1}$ pulsed electric fields at 30 K. The photocurrent was not collected at the dashed line region. **e**, Temperature-dependent ferroelectric hysteresis loop measured by the zero-bias photocurrent method. In this figure, left and right spin chirality are represented as \circlearrowleft (red) and \circlearrowright (green); ferroelectric polarization along [100] is represented as purple arrows \uparrow and \downarrow .

CPGE has a maximum at 680 nm, near the charge-transfer gap of NiI_2 (Extended Data Figs. 9a–d and 10i,j). Apart from the CPGE current associated with circularly polarized light, there is also a spin-independent photocurrent when the incident light is linearly polarized. The total measured photocurrent can be expressed as $I_{\text{total}}(\phi) = C \sin(2\phi) + L_1 \sin(4\phi) + L_2 \cos(4\phi) + D$, in which ϕ is the quarter-wave plate angle, C is the CPGE coefficient, L_1 and L_2 are the linear photogalvanic effect (LPGE) coefficients and the constant D contains other effects, such as photovoltaic effect at the contacts, Dember effect and photon drag effects^{56–59} (see Supplementary Information Section 5 for symmetry analysis of photogalvanic effects). The constant D is subtracted in the angular dependence for clarity and the fitting parameters are listed in the Extended Data Table 1.

The NiI_2 device was first field-cooled to 30 K in the presence of an electric field of 1 MV m^{-1} along the ferroelectric polarization direction, which selects the left chiral spin helix ground state (Fig. 4a–c). Figure 4a shows the temperature-dependent photocurrent along Q_y , when the polarization of incident light is toggled between left and right circular polarization (LCP and RCP, respectively). In the multiferroic phase below 60 K, there is a clear jump of the photocurrent when switching between LCP and RCP. This jump vanishes at the transition temperature. The overall photocurrent amplitude also decreases as temperature is increased, which indicates the magnetic origin of the photocurrent. Figure 4b shows the angular dependence of the photocurrent along Q_y , showing a higher peak when illuminated with

LCP light compared with RCP. This dependence of the photocurrent response on photon helicity is a consequence of the odd-parity spin polarization schematically shown in Fig. 4c. Because LCP and RCP are related by a time-reversal operation, whenever LCP preferentially excites photocarriers with negative momentum along Q_y , RCP must preferentially excite photocarriers with positive momentum, and vice versa. This effect leads to a non-zero CPGE. The NiI_2 device was then field-cooled at -1 MV m^{-1} , corresponding to a right chiral spin helix (Fig. 4d–f). Figure 4d shows that the relative amplitude of the photocurrent between LCP and RCP is reversed with respect to the case of the left chiral spin helix in Fig. 4a, suggesting the switching of the odd-parity spin polarization. The angular dependence in Fig. 4e also shows the switching of the CPGE coefficient when compared with Fig. 4b, now with a higher peak at RCP than LCP, consistent with the band diagram in Fig. 4f.

By contrast, the photocurrent along the ferroelectric polarization direction [100] hardly shows any difference between LCP and RCP, as shown in Fig. 4h. The analysis of the angular dependence reveals that the CPGE coefficient in this case is approximately two orders of magnitude lower than that along Q_y . As we found in the symmetry analysis and confirmed by the DFT results, the spin polarization is expected to be symmetric along the C_{2x} axis, thereby showing vanishing CPGE, as illustrated in Fig. 4i. The observation of CPGE and its switching behaviour is strong evidence of odd-parity spin polarization and its direct coupling to ferroelectric polarization in NiI_2 .

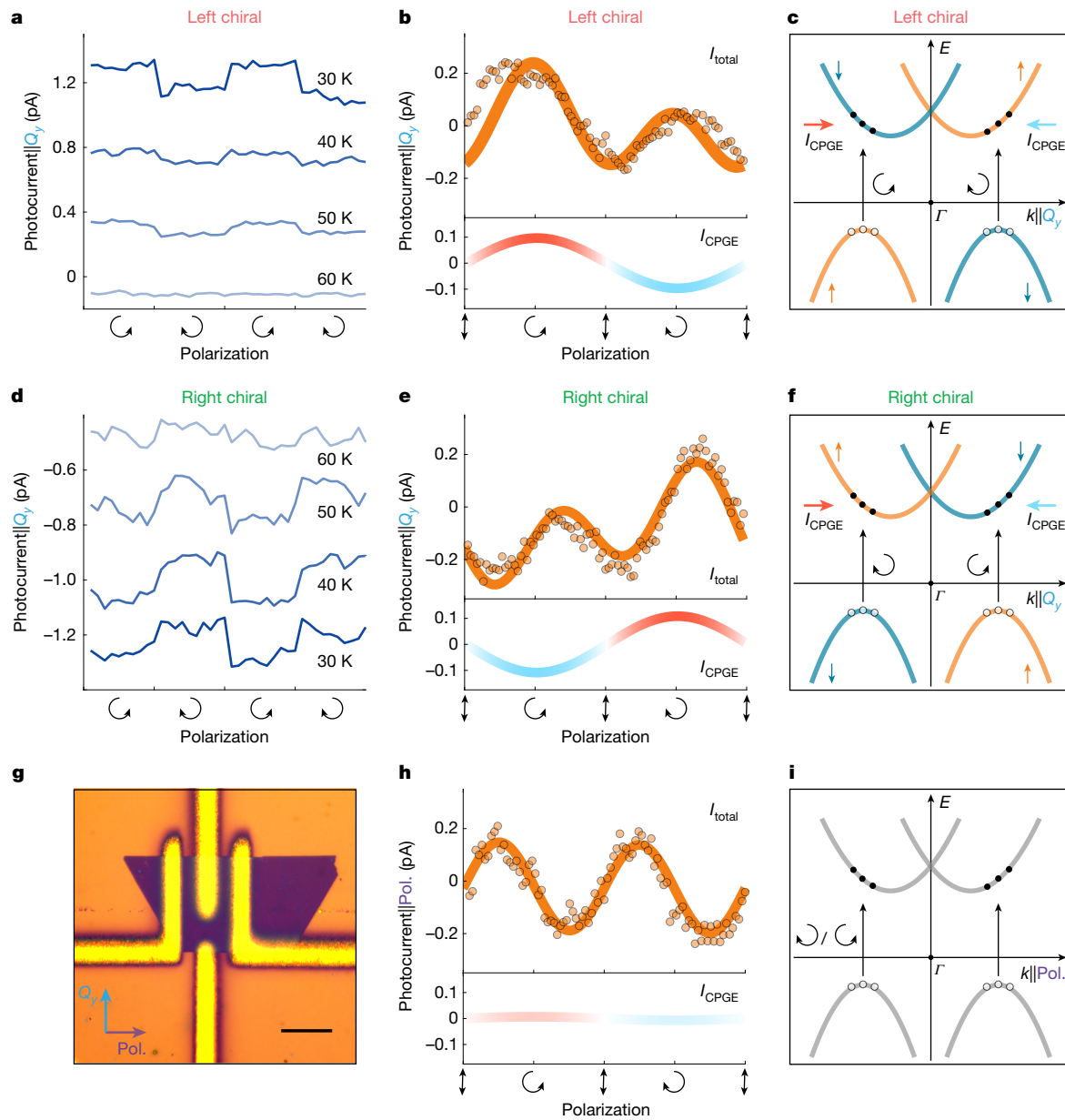


Fig. 4 | CPGE in Nil_2 . **a**, Temperature-dependent CPGE along Q_y for the left chiral spin helix. **b**, Polarization-dependent photocurrent along the Q_y direction shows a higher peak near LCP than RCP. **c**, Schematic spin polarization of the spin helix in Nil_2 , highlighting its antisymmetric character along the Q_y direction, which leads to a non-vanishing CPGE. **d**, Temperature-dependent CPGE along Q_y for the right chiral spin helix. **e**, Polarization-dependent photocurrent along the Q_y direction shows a higher peak near RCP than LCP. **f**, As the spin chirality switches, the spin polarization along Q_y also switches, leading to an opposite CPGE

coefficient compared with **c, g**. **g**, Optical image of the Nil_2 CPGE device. Scale bar, 10 μm . **h**, Polarization-dependent photocurrent along the ferroelectric polarization direction does not show a discernible difference between LCP and RCP, implying that the CPGE is vanishingly small. **i**, The spin polarization of the spin helix in Nil_2 is symmetric along the Pol. direction, leading to a vanishing CPGE. The photocurrent generated from CPGE is labelled as I_{CPGE} ; ferroelectric polarization is labelled as Pol.; left and right circularly polarized light are represented as \circlearrowleft (LCP) and \circlearrowright (RCP).

Discussion

The observation of a robust odd-parity spin polarization in a type II multiferroic with predominantly non-relativistic origin opens new opportunities for developing ultrafast, energy-efficient and high-endurance antiferromagnetic spintronic devices with substantial electrical readout capabilities. The electromagnon energy of the spin helix in Nil_2 is around 1 THz (refs. 33,60), suggesting the potential for picosecond-scale switching of helimagnetic order⁴³. Although the spin-induced ferroelectric polarization is around four orders of magnitude lower than that of BaTiO_3 (a conventional ionic ferroelectric oxide), its coercive field is only half of that in BaTiO_3 (ref. 61). Consequently, the

switching energy can be expected to be up to five orders of magnitude lower. Furthermore, devices based on improper ferroelectrics of purely electronic origin are characterized by much higher endurance. Last, because of its dominant non-relativistic origin, the spin splitting of an odd-parity magnet can be as large as the eV scale, potentially resulting in enhanced electrical readout for spintronic devices²⁰.

Conclusion

The reported results represent, to our knowledge, the first observation of an electrically switchable p -wave magnet. Group-theory analysis and DFT calculations confirm the odd-parity character of the spin

polarization even in the absence of SOC. These findings open a new frontier to realize symmetry-protected voltage-based switching of non-relativistic spin polarization in a compensated magnet.

Online content

Any methods, additional references, Nature Portfolio reporting summaries, source data, extended data, supplementary information, acknowledgements, peer review information; details of author contributions and competing interests; and statements of data and code availability are available at <https://doi.org/10.1038/s41586-025-09034-7>.

1. Baltz, V. et al. Antiferromagnetic spintronics. *Rev. Mod. Phys.* **90**, 015005 (2018).
2. Olejnik, K. et al. Terahertz electrical writing speed in an antiferromagnetic memory. *Sci. Adv.* **4**, eaar3566 (2018).
3. Šmejkal, L., Sinova, J. & Jungwirth, T. Emerging research landscape of altermagnetism. *Phys. Rev. X* **12**, 040501 (2022).
4. Šmejkal, L., Sinova, J. & Jungwirth, T. Beyond conventional ferromagnetism and antiferromagnetism: a phase with nonrelativistic spin and crystal rotation symmetry. *Phys. Rev. X* **12**, 031042 (2022).
5. Hellenes, A. B., Jungwirth, T., Sinova, J. & Šmejkal, L. P-wave magnets. Preprint at <https://arxiv.org/abs/2309.01607> (2024).
6. Krempasky, J. et al. Altermagnetic lifting of Kramers spin degeneracy. *Nature* **626**, 517–522 (2024).
7. Amin, O. J. et al. Nanoscale imaging and control of altermagnetism in MnTe. *Nature* **636**, 348–353 (2024).
8. Wadley, P. et al. Electrical switching of an antiferromagnet. *Science* **351**, 587–590 (2016).
9. Yan, H. et al. Electric-field-controlled antiferromagnetic spintronic devices. *Adv. Mater.* **32**, 1905603 (2020).
10. Tokura, Y., Seki, S. & Nagaosa, N. Multiferroics of spin origin. *Rep. Prog. Phys.* **77**, 076501 (2014).
11. Fiebig, M., Lottermoser, T., Meier, D. & Trassin, M. The evolution of multiferroics. *Nat. Rev. Mater.* **1**, 16046 (2016).
12. Cheong, S.-W. & Mostovoy, M. Multiferroics: a magnetic twist for ferroelectricity. *Nat. Mater.* **6**, 13–20 (2007).
13. Kurumaji, T. Spiral spin structures and skyrmions in multiferroics. *Phys. Sci. Rev.* **5**, 20190016 (2020).
14. Masuda, R., Kaneko, Y., Tokura, Y. & Takahashi, Y. Electric field control of natural optical activity in a multiferroic helimagnet. *Science* **372**, 496–500 (2021).
15. Chen, X. et al. Unconventional magnons in collinear magnets dictated by spin space groups. *Nature* **640**, 349–354 (2025).
16. Hayami, S., Yanagi, Y. & Kusunose, H. Momentum-dependent spin splitting by collinear antiferromagnetic ordering. *J. Phys. Soc. Jpn.* **88**, 123702 (2019).
17. Yuan, L.-D., Wang, Z., Luo, J.-W., Rashba, E. I. & Zunger, A. Giant momentum-dependent spin splitting in centrosymmetric low-Z antiferromagnets. *Phys. Rev. B* **102**, 014422 (2020).
18. Yuan, L.-D., Wang, Z., Luo, J.-W. & Zunger, A. Prediction of low-Z collinear and noncollinear antiferromagnetic compounds having momentum-dependent spin splitting even without spin-orbit coupling. *Phys. Rev. Mater.* **5**, 014409 (2021).
19. Chen, X. et al. Octupole-driven magnetoresistance in an antiferromagnetic tunnel junction. *Nature* **613**, 490–495 (2023).
20. Qin, P. et al. Room-temperature magnetoresistance in an all-antiferromagnetic tunnel junction. *Nature* **613**, 485–489 (2023).
21. Zhu, Y.-P. et al. Observation of plaid-like spin splitting in a noncoplanar antiferromagnet. *Nature* **626**, 523–528 (2024).
22. Cheong, S.-W. & Huang, F.-T. Altermagnetism with non-collinear spins. *npj Quantum Mater.* **9**, 13 (2024).
23. Brekke, B., Sukhachov, P., Giil, H. G., Brataas, A. & Linder, J. Minimal models and transport properties of unconventional p-wave magnets. *Phys. Rev. Lett.* **133**, 236703 (2024).
24. Yamada, R. et al. Gapping the spin-nodal planes of an anisotropic p-wave magnet to induce a large anomalous Hall effect. Preprint at <https://arxiv.org/abs/2502.10386> (2025).
25. Maeda, K., Lu, B., Yada, K. & Tanaka, Y. Theory of tunneling spectroscopy in unconventional p-wave magnet-superconductor hybrid structures. *J. Phys. Soc. Jpn.* **93**, 114703 (2024).
26. Katsura, H., Nagaosa, N. & Balatsky, A. V. Spin current and magnetoelectric effect in noncollinear magnets. *Phys. Rev. Lett.* **95**, 057205 (2005).
27. Sergienko, I. A. & Dagotto, E. Role of the Dzyaloshinskii-Moriya interaction in multiferroic perovskites. *Phys. Rev. B* **73**, 094434 (2006).
28. Babkovich, P. et al. Electric field control of chiral magnetic domains in the high-temperature multiferroic CuO. *Phys. Rev. B* **85**, 134428 (2012).
29. Stein, J. et al. Control of chiral magnetism through electric fields in multiferroic compounds above the long-range multiferroic transition. *Phys. Rev. Lett.* **119**, 177201 (2017).
30. Sagayama, H. et al. Observation of spin helicity using nonresonant circularly polarized X-ray diffraction analysis. *J. Phys. Soc. Jpn.* **79**, 043711 (2010).
31. Yamasaki, Y. et al. Electric control of spin helicity in a magnetic ferroelectric. *Phys. Rev. Lett.* **98**, 147204 (2007).
32. Kurumaji, T. et al. Magnetoelectric responses induced by domain rearrangement and spin structural change in triangular-lattice helimagnets Ni₂ and Co₂. *Phys. Rev. B* **87**, 014429 (2013).
33. Song, Q. et al. Evidence for a single-layer van der Waals multiferroic. *Nature* **602**, 601–605 (2022).
34. Amini, M. et al. Atomic-scale visualization of multiferroicity in monolayer Ni₂. *Adv. Mater.* **36**, 2311342 (2024).
35. Friedt, J. M., Sanchez, J. P. & Shenoy, G. K. Electronic and magnetic properties of metal diiodides M₂ (M=V, Cr, Mn, Fe, Co, Ni, and Cd) from ¹²⁹I Mössbauer spectroscopy. *J. Chem. Phys.* **65**, 5093–5102 (1976).
36. Amoroso, D., Barone, P. & Picozzi, S. Spontaneous skyrmionic lattice from anisotropic symmetric exchange in a Ni-halide monolayer. *Nat. Commun.* **11**, 5784 (2020).
37. Botana, A. S. & Norman, M. R. Electronic structure and magnetism of transition metal dihalides: bulk to monolayer. *Phys. Rev. Mater.* **3**, 44001 (2019).
38. Fumega, A. O. & Lado, J. Microscopic origin of multiferroic order in monolayer Ni₂. *2D Mater.* **9**, 025010 (2022).
39. Kuindersma, S., Sanchez, J. & Haas, C. Magnetic and structural investigations on Ni₂ and Co₂. *Physica B+C* **111**, 231–248 (1981).
40. Tseng, Y., Occhipinti, C. A. et al. Shear-mediated stabilization of spin spiral order in multiferroic Ni₂. *Adv. Mater.* **37**, 2417434 (2025).
41. Arima, T.-h. Ferroelectricity induced by proper-screw type magnetic order. *J. Phys. Soc. Jpn.* **76**, 073702 (2007).
42. Xiang, H. J., Kan, E. J., Zhang, Y., Whangbo, M.-H. & Gong, X. G. General theory for the ferroelectric polarization induced by spin-spiral order. *Phys. Rev. Lett.* **107**, 157202 (2011).
43. Gao, F. Y. et al. Giant chiral magnetoelectric oscillations in a van der Waals multiferroic. *Nature* **632**, 273–279 (2024).
44. Braunecker, B., Japaridze, G. I., Klinovaja, J. & Loss, D. Spin-selective Peierls transition in interacting one-dimensional conductors with spin-orbit interaction. *Phys. Rev. B* **82**, 045127 (2010).
45. Choy, T.-P., Edge, J. M., Akhmerov, A. R. & Beenakker, C. W. J. Majorana fermions emerging from magnetic nanoparticles on a superconductor without spin-orbit coupling. *Phys. Rev. B* **84**, 195442 (2011).
46. Martin, I. & Morpurgo, A. F. Majorana fermions in superconducting helical magnets. *Phys. Rev. B* **85**, 144505 (2012).
47. Egger, R. & Flensberg, K. Emerging Dirac and Majorana fermions for carbon nanotubes with proximity-induced pairing and spiral magnetic field. *Phys. Rev. B* **85**, 235462 (2012).
48. Nadj-Perge, S., Drozdov, I. K., Bernevig, B. A. & Yazdani, A. Proposal for realizing Majorana fermions in chains of magnetic atoms on a superconductor. *Phys. Rev. B* **88**, 020407 (2013).
49. Cheong, S.-W. & Huang, F.-T. Kinetomagnetism of chirality and its applications. *Appl. Phys. Lett.* **125**, 060501 (2024).
50. Masuda, H. et al. Room temperature chirality switching and detection in a helimagnetic MnAu₂ thin film. *Nat. Commun.* **15**, 1999 (2024).
51. Chen, G., Khosrovian, M., Lado, J. L. & Ramires, A. Designing spin-textured flat bands in twisted graphene multilayers via helimagnet encapsulation. *2D Mater.* **9**, 024002 (2022).
52. Sandratskii, L. Noncollinear magnetism in itinerant-electron systems: theory and applications. *Adv. Phys.* **47**, 91–160 (1998).
53. Mayo, A. H. et al. Band asymmetry-driven nonreciprocal electronic transport in a helimagnetic semimetal α -EuP₃. *Proc. Natl. Acad. Sci.* **122**, e2405839122 (2025).
54. Grinberg, I. et al. Perovskite oxides for visible-light-absorbing ferroelectric and photovoltaic materials. *Nature* **503**, 509–512 (2013).
55. Matsubara, M. et al. Magnetoelectric domain control in multiferroic TbMnO₃. *Science* **348**, 1112–1115 (2015).
56. Zhang, L. et al. Room-temperature electrically switchable spin-valley coupling in a van der Waals ferroelectric halide perovskite with persistent spin helix. *Nat. Photon.* **16**, 529–537 (2022).
57. Niu, C. et al. Tunable circular photogalvanic and photovoltaic effect in 2D tellurium with different chirality. *Nano Lett.* **23**, 3599–3606 (2023).
58. Wang, S. et al. Circular photogalvanic effect in oxide two-dimensional electron gases. *Phys. Rev. Lett.* **128**, 187401 (2022).
59. McIver, J., Hsieh, D., Steinberg, H., Jarillo-Herrero, P. & Gedik, N. Control over topological insulator photocurrents with light polarization. *Nat. Nanotechnol.* **7**, 96–100 (2012).
60. Kim, J. H. et al. Terahertz evidence of electromagnon excitations in the multiferroic van der Waals insulator Ni₂. *Phys. Rev. B* **108**, 064414 (2023).
61. Martin, L. W. & Rappe, A. M. Thin-film ferroelectric materials and their applications. *Nat. Rev. Mater.* **2**, 16087 (2017).

Publisher's note Springer Nature remains neutral with regard to jurisdictional claims in published maps and institutional affiliations.

Springer Nature or its licensor (e.g. a society or other partner) holds exclusive rights to this article under a publishing agreement with the author(s) or other rightsholder(s); author self-archiving of the accepted manuscript version of this article is solely governed by the terms of such publishing agreement and applicable law.

© The Author(s), under exclusive licence to Springer Nature Limited 2025

Methods

Growth and characterization of NiI_2 crystals

NiI_2 thin flakes were grown on 300-nm SiO_2/Si through physical vapour deposition (PVD) in a horizontal single-zone furnace equipped with a 0.5-inch-diameter quartz tube at ambient pressure⁶². In a typical synthesis, 0.2 g of NiI_2 powder (99.5%, anhydrous, Alfa Aesar) were positioned at the centre of the furnace as the source material and the SiO_2/Si substrate was placed downstream at the maximum temperature gradient point. The furnace was purged by pumping the quartz tube to below 0.5 Torr and then refilled with 99.99% Ar gas twice. The furnace was heated to 430 °C in 15 min and held at that temperature for 10 min. After the growth, the SiO_2/Si substrate was taken out immediately and stored inside a nitrogen-filled glovebox ($\text{O}_2 < 0.2 \text{ ppm}$, $\text{H}_2\text{O} < 0.5 \text{ ppm}$). The sample thickness was determined by atomic force microscopy (AFMWorkshop HR) measurements performed inside a separate nitrogen-filled glovebox ($\text{O}_2 < 100 \text{ ppm}$, $\text{H}_2\text{O} < 1 \text{ ppm}$), using a silicon probe in tapping mode. The crystallographic orientation of NiI_2 flakes is determined by electron diffraction of transmission electron microscopy (FEI, Technai). Single-crystal NiI_2 was grown by chemical vapour transport (CVT), from elemental precursors with molar ratio $\text{Ni:I} = 1:2$, at a temperature gradient 650 °C to 570 °C. The magnetic susceptibility was measured during field cooling at 0.9 T applied out of plane, using a Magnetic Property Measurement System (MPMS-3, Quantum Design). X-ray diffraction of CVT-grown crystals was performed in Bragg geometry using Cu K α radiation (PANalytical).

Device fabrication

The device for BPVE measurement was fabricated by depositing Ti (5 nm)/Au (30 nm) electrodes on SiO_2 (300 nm)/Si substrate using standard photolithography methods. A PVD-grown NiI_2 flake was picked up and dropped down across the electrodes using a polymer-based transfer technique. To minimize the exposure to moisture, the polymer was dissolved in anhydrous chloroform inside the glovebox. The NiI_2 CPGE device was fabricated by transferring gold contacts on top of the sample. An ultrathin Si (50 μm thick) wafer with designed pattern was fabricated using deep reactive ion etching. Gold contacts (50 nm thick) without adhesion layer were deposited through the etched region onto the other SiO_2/Si handle wafer. These gold contacts without adhesion layer can be transferred using the standard polymer-based transfer technique.

Linear dichroism measurements

A supercontinuum light source (SuperK, NKT Photonics) monochromatized to $\lambda = 633 \text{ nm}$ and a bandwidth of approximately 1 nm was used as excitation for angular-dependent linear dichroism measurements. All measurements were performed at normal incidence in a closed-cycle optical cryostat (OptiCool, Quantum Design). Linear dichroism measurements were performed with a photoelastic modulator (PEM; PEM-200, Hinds Instruments) on the incident path of the optical set-up. The beam incident on the PEM is prepared in linear polarization with an angle of 45° with respect to the PEM fast axis and amplitude modulated with a mechanical chopper. The PEM retardance was set to 0.5λ to modulate the incident polarization between ±45° linear polarization states. The light is then focused onto the sample using a 50× objective lens. The backscattered light is measured by an amplified photodiode (PDA100A2, Thorlabs), whose output is connected to a lock-in amplifier (SR865A, Stanford Instruments) referenced to the second harmonic of the fundamental PEM frequency $f = 50 \text{ kHz}$. The total reflectance of the sample, used as a normalization, is monitored by a second lock-in amplifier referenced to the chopping frequency $f = 557 \text{ Hz}$. This set-up has a sensitivity down to 10 μrad .

To perform angular-dependent linear dichroism measurements, the angle of the perpendicular linear polarization states produced by the PEM is varied across the crystal using a zero-order half-wave

plate placed just before the objective. To ensure that the angular dependence is recorded from a uniform, mono-domain region of the sample, linear dichroism microscopy images were first recorded at $T = 30 \text{ K}$. The sample was held at this temperature for the duration of the angular-dependent measurements to maintain the same distribution of birefringent domains.

To perform linear dichroism imaging, the 50× objective is mounted on a closed-loop motorized stage. The polarization of incident light is aligned along the [120] direction by rotating the half-wave plate. The scanning of linear dichroism was repeated at 30 K for two different cooling cycles to confirm the memory of the domain distribution.

Cross-polarized imaging was performed with a broadband visible LED light source, a standard CMOS-based monochrome camera and Glan-Thompson Polarizers on both the input and output light paths in reflection geometry. A detuning of 0.5(2.0)° from a cross-polarized configuration was used to maximize the contrast from birefringent domains.

Raman spectroscopy measurements

Polarized Raman experiments were performed in a backscattering geometry using a confocal microscope spectrometer (LabRAM HR Evolution, Horiba) with a 50× objective lens and 532-nm laser excitation at a power of 40 μW . Scattered light was dispersed by a 1,800 lines per millimetre grating and detected with a liquid nitrogen cooled charge-coupled device camera. The spectrometer integration time was 30 min and each scan was taken twice and then averaged before analysis. An achromatic quarter-wave plate was placed in front of the objective with fast axis oriented at ±45° with respect to the incident linear polarization for LCP/RCP circular incident polarization, respectively. For the reported circularly polarized spectra, no analysing polarizer was used.

SHG measurements

In second-harmonic generation (SHG) measurements, an objective lens (LMPlanFL-N 50×, Olympus) was used to focus an ultrashort laser beam onto the sample located in a cryostat (ST-500, Janis). The laser fluence was set to 1 mJ cm^{-2} . On reflection, the second-harmonic component of the beam radiated from sample was selected out by a dichroic mirror and a monochromator with 2-nm spectral resolution. The second-harmonic photons were counted using a photomultiplier tube (Hamamatsu) and a dual-channel gated photon counter (SR400, Stanford Research).

Transport measurements

The sub-picoampere current was measured using electrometers (B2985B, Keysight) in a cryostat (OptiCool, Quantum Design). The electrical connection uses a triaxial cable (three layers work as ground/shield/pin) from the electrometer to the cryostat. A coaxial cable (shield/pin) is used inside the cryostat, whereas the whole cryostat works as a ground layer. This triaxial connection is retained all the way from the electrometer to sample to reach a femtoampere noise floor. A supercontinuum laser (SuperK, NKT Photonics) monochromatized by a prism and a bandwidth of approximately 1 nm was used for the photocurrent spectra measurement. The laser was focused using a 20× objective to form a 5-μm-diameter illumination on the NiI_2 sample for the zero-bias photocurrent (BPVE in Fig. 3) measurement. To perform temperature-dependent zero-bias photocurrent measurement, the sample was first field-cooled from 80 K to 30 K in the dark. For the BPVE and CPGE measurements, the field-cooling strengths ±2 MV m^{-1} and ±1 MV m^{-1} were applied, respectively. Applying a higher electric field could show a leakage current at 80 K. Subsequently, the photocurrent was collected at zero bias while slowly warming at a rate of 0.5 K min^{-1} , to avoid thermocurrent effects. The temperature-dependent zero-bias photocurrent measurements in the CPGE devices (Extended Data Figs. 8f and 10e) subtracted a constant background arising from the second pair of electrodes. For the ferroelectric hysteresis loop

- measurements, the laser shutter was closed while a 10-s pulsed electric field was applied, to avoid photocurrent overshoot and minimize the risk of burning the device. At zero bias, the laser shutter was open to help stabilize the photocurrent and the zero-bias photocurrent was measured after a 60-s wait time. For pyroelectric current measurements, the edge of a 5 mm × 5 mm × 0.1 mm single-crystal NiI_2 was cut to expose a fresh surface and the silver paste was applied to form electrical contact. The sample was first field-cooled to the base temperature at a bias of ±100 V and then the current was measured in the dark at a warming speed of 3–4 K min⁻¹ from 20 K to 80 K.
- To perform CPGE measurement, circularly polarized light was prepared by placing a linear polarizer followed by an achromatic quarter-wave plate (AQWP05M-600, Thorlabs) before the objective. The laser was focused using a 50× objective to form a 2-μm-diameter illumination on the NiI_2 sample. The circularly polarized photocurrent was collected by rotating the fast axis of the quarter-wave plate at 45° and −45° to the linear polarizer.

First-principles modelling of spin helices

The electronic structure of spin helices in NiI_2 monolayer was calculated using the non-collinear DFT framework of the Vienna Ab initio Simulation Package (VASP) based on pseudopotentials and plane waves⁶³. The structure of NiI_2 monolayer was modelled with a lattice parameter of $a = 3.97 \text{ \AA}$, Ni–I bond length of 2.746 Å and 25 Å of separation along the c axis (zaxis) to ensure the sufficient vacuum between periodic replicas. The effects of electronic exchange and correlation were described within the generalized gradient approximation using the Perdew–Burke–Ernzerhof functional⁶⁴. The projector-augmented wave⁶⁵ pseudopotentials with Ni 3p, 3d, 4s and 1s, 5p states in the valence were used and the Kohn–Sham wavefunctions were expanded on a plane-wave basis set with a cut-off of 500 eV. To keep the same level of accuracy for spin helices whose modelling requires using different supercells (Extended Data Figs. 4–6), in each case, the first Brillouin zone was sampled with a k -points mesh of density $\approx 0.009 \text{ \AA}^{-2}$. Band structure and spin texture plots were produced using the PyProcar package⁶⁶. Atomic Simulation Environment⁶⁷ and XCrySDen⁶⁸ software were used for setting up DFT calculations and visualizing the spin helices.

Data availability

The datasets generated and/or analysed during the present study are available at <https://doi.org/doi:10.7910/DVN/MSCHDT> (ref. 69).

62. Liu, H. et al. Vapor deposition of magnetic van der Waals NiI_2 crystals. *ACS Nano* **14**, 10544–10551 (2020).
63. Kresse, G. & Furthmüller, J. Efficient iterative schemes for *ab initio* total-energy calculations using a plane-wave basis set. *Phys. Rev. B* **54**, 11169 (1996).
64. Perdew, J. P., Burke, K. & Ernzerhof, M. Generalized gradient approximation made simple. *Phys. Rev. Lett.* **77**, 3865 (1996).
65. Blöchl, P. E. Projector augmented-wave method. *Phys. Rev. B* **50**, 17953 (1994).
66. Herath, U. et al. PyProcar: a Python library for electronic structure pre/post-processing. *Comput. Phys. Commun.* **251**, 107080 (2020).
67. Larsen, A. H. et al. The atomic simulation environment—a Python library for working with atoms. *J. Phys. Condens. Matter* **29**, 273002 (2017).
68. Kokalj, A. XCrySDen—a new program for displaying crystalline structures and electron densities. *J. Mol. Graph. Model.* **17**, 176–179 (1999).
69. Song, Q. Electrical switching of an unconventional odd-parity magnet. *Harvard Dataverse* <https://doi.org/doi:10.7910/DVN/MSCHDT> (2025).

Acknowledgements The authors thank J. Linder, L. Šmejkal, T. Jungwirth and J. Sinova for insightful discussions on the spin group symmetry analysis. This work was supported by the National Science Foundation (NSF) under grant no. DMR-2405560 (photocurrent spectroscopy and device fabrication) and the Department of Energy, Office of Science, Office of Basic Energy Sciences, under award number DE-SC0019126 (sample synthesis). The cryomagnet used in this work (OptiCool, Quantum Design) was acquired with support from the Air Force Office of Scientific Research under the Defense University Research Instrumentation Program (DURIP) grant FA9550-22-1-0130. S.-W.C. was supported by the DOE under grant no. DOE-DE-FG02-07ER46382. R.M.F. (theoretical model) was supported by the Air Force Office of Scientific Research under award no. FA9550-21-1-0423. J.W.F.V. was supported by NSF award no. DMR-2144352. D.S.A. was supported by NSF grant no. DMR-2410182 and the Yale Mossman Postdoctoral Fellowship. S.S. acknowledges the financial support provided by the Ministry of Education, Science and Technological Development of the Republic of Serbia. S.S., P.B., A.D. and S.P. acknowledge the CINECA award under the ISCRA initiative for the availability of high-performance computing resources and support. S.P. acknowledges funding through the Next-Generation EU programme PRIN-2022 project “SORBET: Spin-ORBit Effects in Two-dimensional magnets” (IT MIUR grant no. 2022ZY8HJY) and the ICSC initiative (National Center for High-Performance Supercomputing, Big Data and Quantum Computing). B.I., E.E. and N.G. acknowledge support from the US Department of Energy, Materials Science and Engineering Division, Office of Basic Energy Sciences (BES DMSE) for the second-harmonic generation measurements.

Author contributions Q.S. and R.C. conceived the project. Q.S. synthesized the NiI_2 crystals, fabricated the devices and performed optical and photocurrent measurements. C.A.O. provided support for optical measurements. S.S., P.B., A.D. and S.P. performed the density functional theory calculations and analysis. Q.S. and S.-W.C. carried out the symmetry analysis. D.S.A., J.W.F.V. and R.M.F. carried out the group-theory analysis. B.I. and E.E. performed second-harmonic generation measurements, supervised by N.G. Q.S., R.M.F. and R.C. wrote the paper, with contributions from all co-authors.

Competing interests The authors declare no competing interests.

Additional information

Supplementary information The online version contains supplementary material available at <https://doi.org/10.1038/s41586-025-09034-7>.

Correspondence and requests for materials should be addressed to Qian Song, Rafael M. Fernandes or Riccardo Comin.

Peer review information *Nature* thanks Bo Peng and the other, anonymous, reviewer(s) for their contribution to the peer review of this work. Peer reviewer reports are available.

Reprints and permissions information is available at <http://www.nature.com/reprints>.

Article

Magnetic Structure	Example	Magnetic order	Spin-Splitting?	Spin-Splitting without SOC?
Ferromagnet	Fe		Yes	Yes
Collinear Compensated Magnets	NiO		No	/
	MnS ₂		Yes	No
	CuMnAs		No	/
	MnTe		Yes	Yes
Non-collinear Compensated Magnets	Mn ₃ X (X= Sn Ge, Ir, Pt)		Yes	Yes
	Helimagnet		Yes	Yes
Non-magnet	Non-centro symmetric lattice	/	Yes	No (Rashba, Weyl ... SOC)



↑ ↓ represent spin up and down,

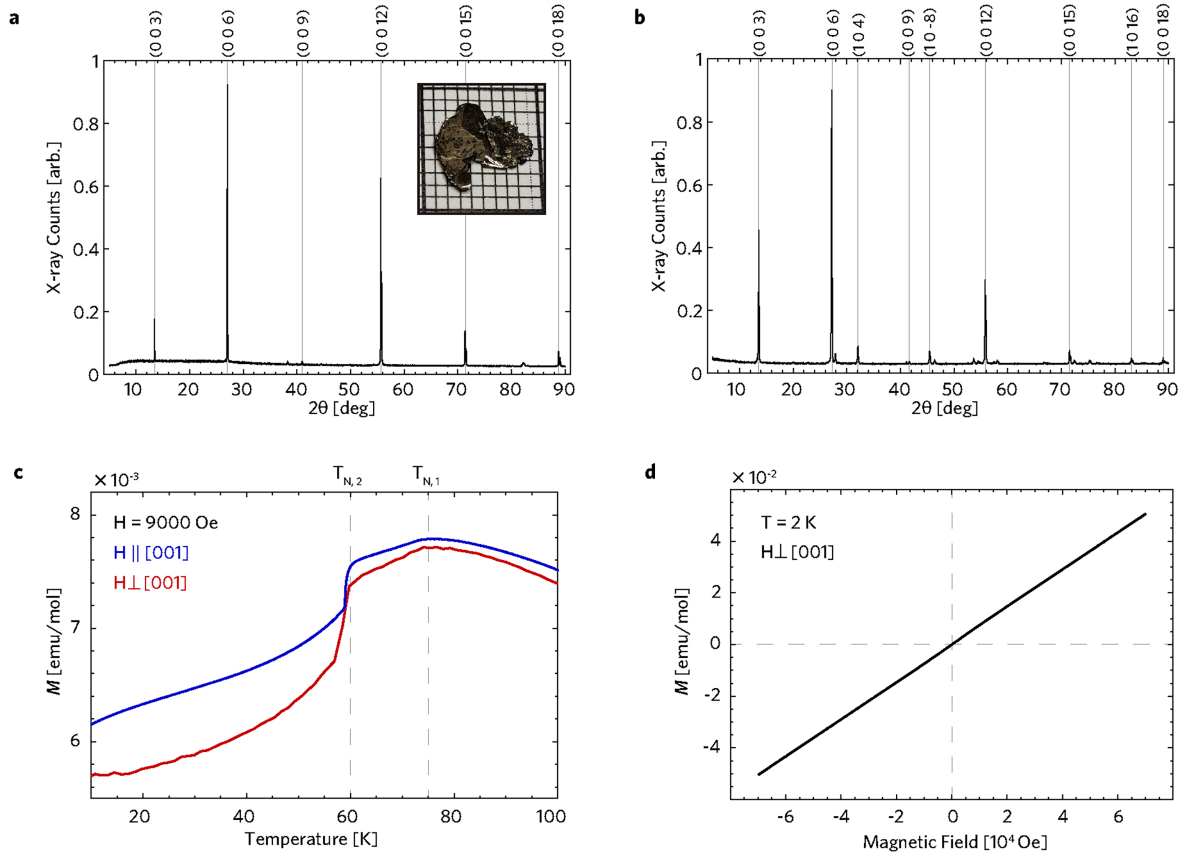


△ ▽ represent surrounding non-magnetic atoms



● ● represent two different local environment for spin

Extended Data Fig. 1 | Spin splitting in different types of magnetically ordered state. Depending on the spin-group symmetries that leave the magnetic configuration invariant, a spin splitting can emerge even in the absence of SOC.

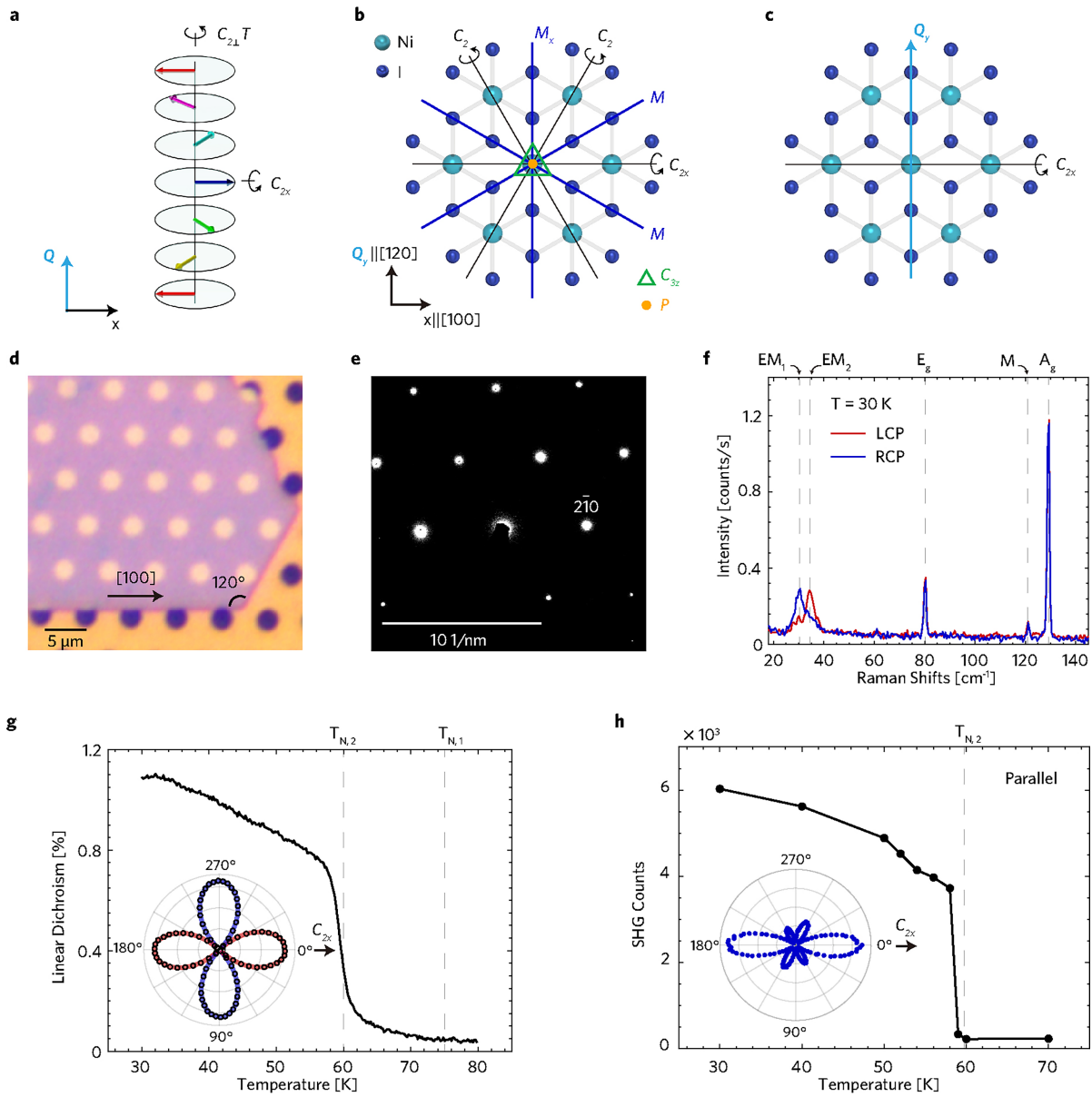


Extended Data Fig. 2 | Structural and magnetic characterization of NiI_2 .

a, X-ray diffraction of a CVD-grown NiI_2 single crystal along the [001] axis. Inset, optical image of NiI_2 single crystal with grid size 1 mm. **b**, X-ray powder diffraction of CVD-grown NiI_2 crystals. **c**, Temperature-dependent magnetic

susceptibility shows two magnetic transitions, first to an antiferromagnetic state at $T_{N,2} = 75$ K and then to a helimagnetic state below $T_{N,1} = 59.5$ K with vanishing magnetization. **d**, Magnetic susceptibility at 2 K shows weak linear response to magnetic field up to 7 T.

Article

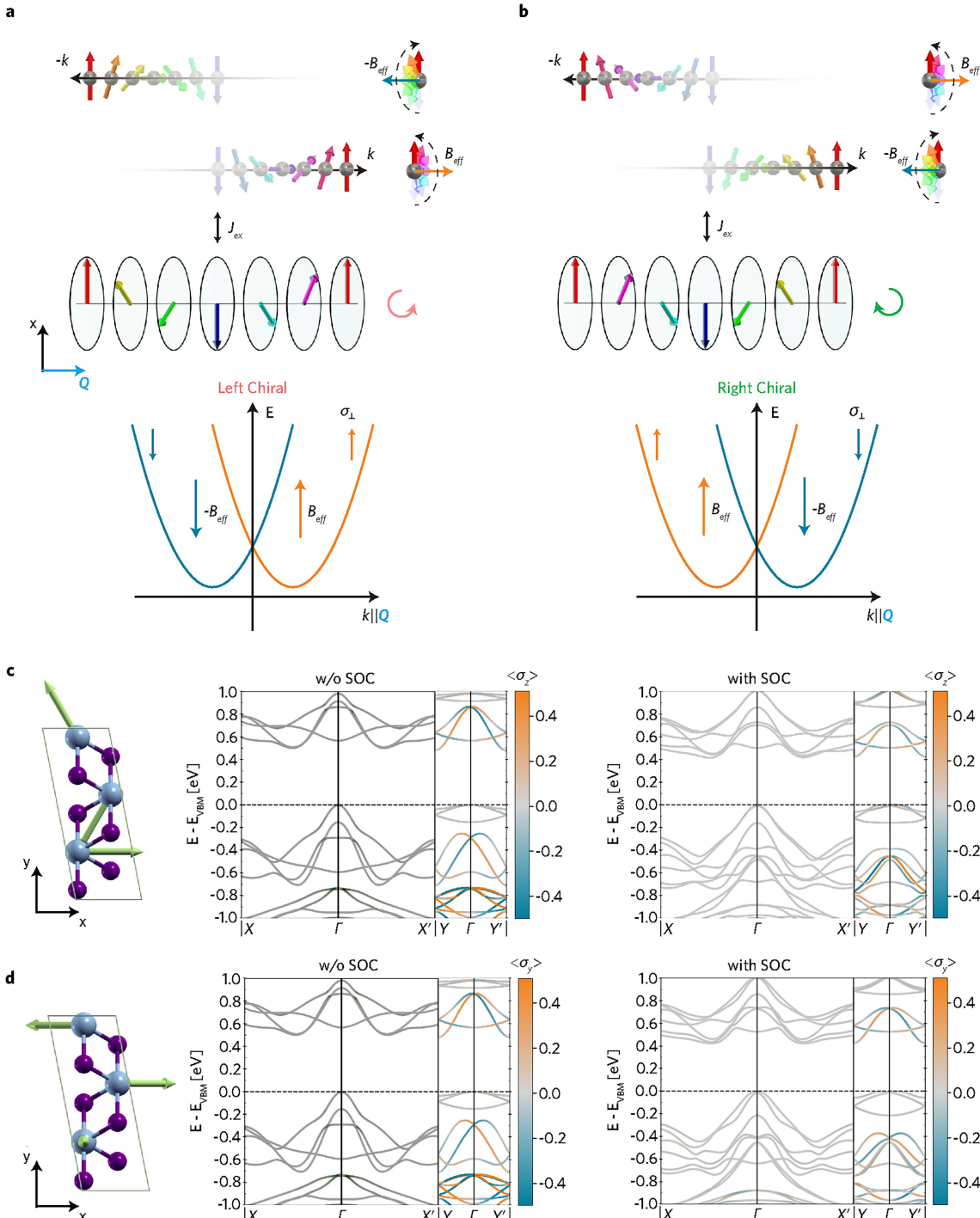


Extended Data Fig. 3 | Structural and optical characterization of NiI_2 .

a, Helical spin structure in a one-dimensional chain has several twofold rotational symmetries $C_{21}T$ and $C_{2\parallel}$ with rotation axes aligned with the local spin, for example, C_{2x} . **b**, NiI_2 crystallizes in $R\bar{3}m$ structure, with three in-plane C_2 axes 60° to each other. The C_{2x} of the helix aligns with the C_{2x} of the lattice. **c**, Embedding the helical spin structure into the $R\bar{3}m$ lattice with propagation vector \mathbf{Q} lying in the $[120]/[001]$ plane results in a single twofold rotational symmetry C_{2x} . **d**, Optical image of a 40-nm-thick PVD-grown NiI_2 flake transferred onto a transmission electron microscopy grid. **e**, Transmission electron microscopy diffraction image is aligned with the optical image in **d**. The long

edge of the PVD-grown NiI_2 flake is confirmed to be the principal axis.

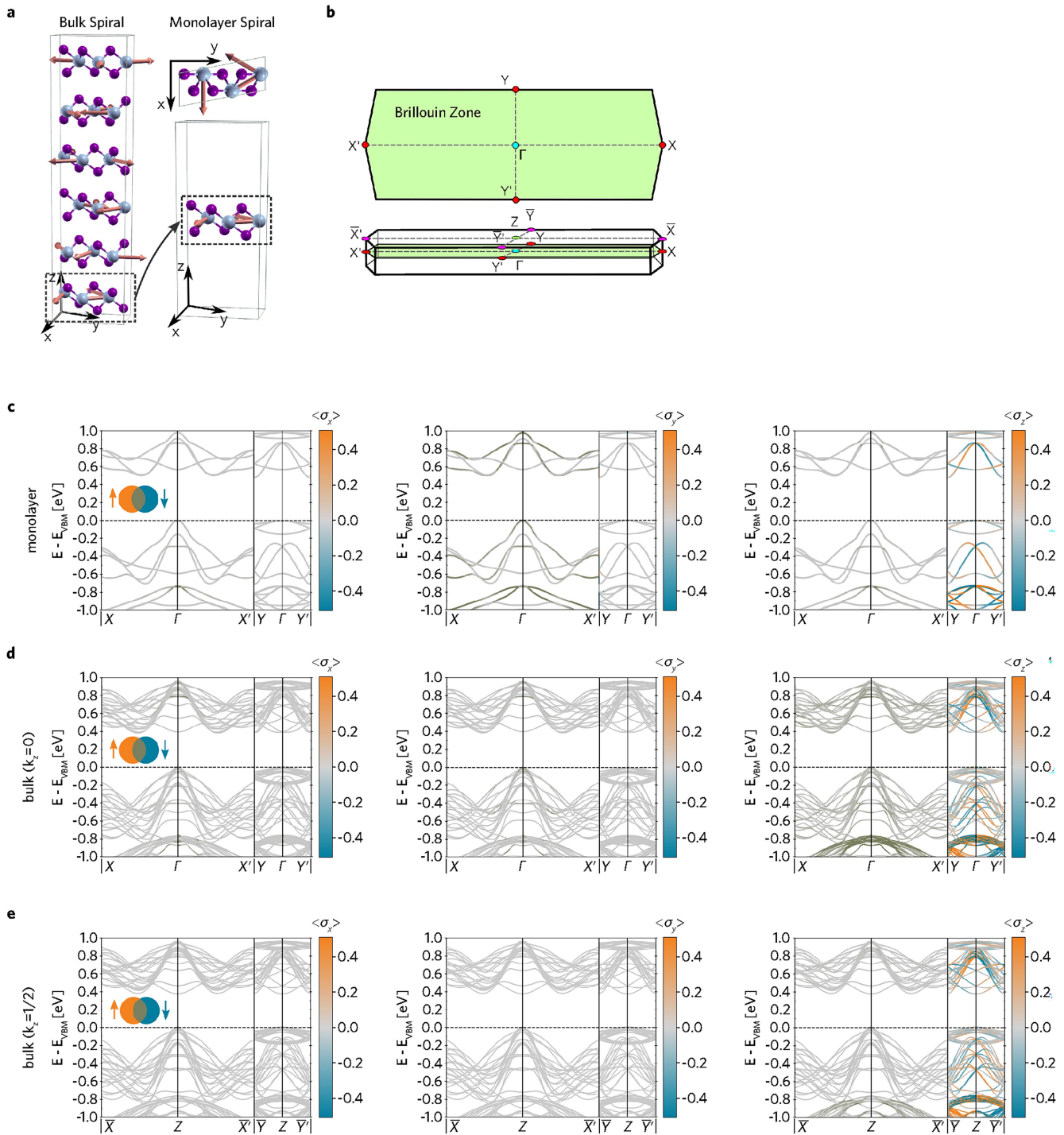
f, Circularly polarized Raman spectroscopy at 30 K on a single-domain region of NiI_2 PVD-grown flake shows circular dichroism in electromagnon modes (EM_1 and EM_2) but not in phonon modes (A_g and E_g) or magnon mode (M). **g**, Temperature-dependent linear dichroism measurement on a single-domain region of PVD-grown NiI_2 flake shows a sharp jump at $T_{N,2} = 59.5 \text{ K}$. The inset shows the angular dependence of linear dichroism at 30 K. **h**, Below bandgap ($\lambda = 991 \text{ nm}$) temperature-dependent SHG in parallel configuration on a single-domain region of PVD-grown NiI_2 flake shows a sharp jump at $T_{N,2} = 59.5 \text{ K}$. The inset shows the angular dependence of SHG at 30 K.



Extended Data Fig. 4 | Schematics of spin splitting in spiral magnets.

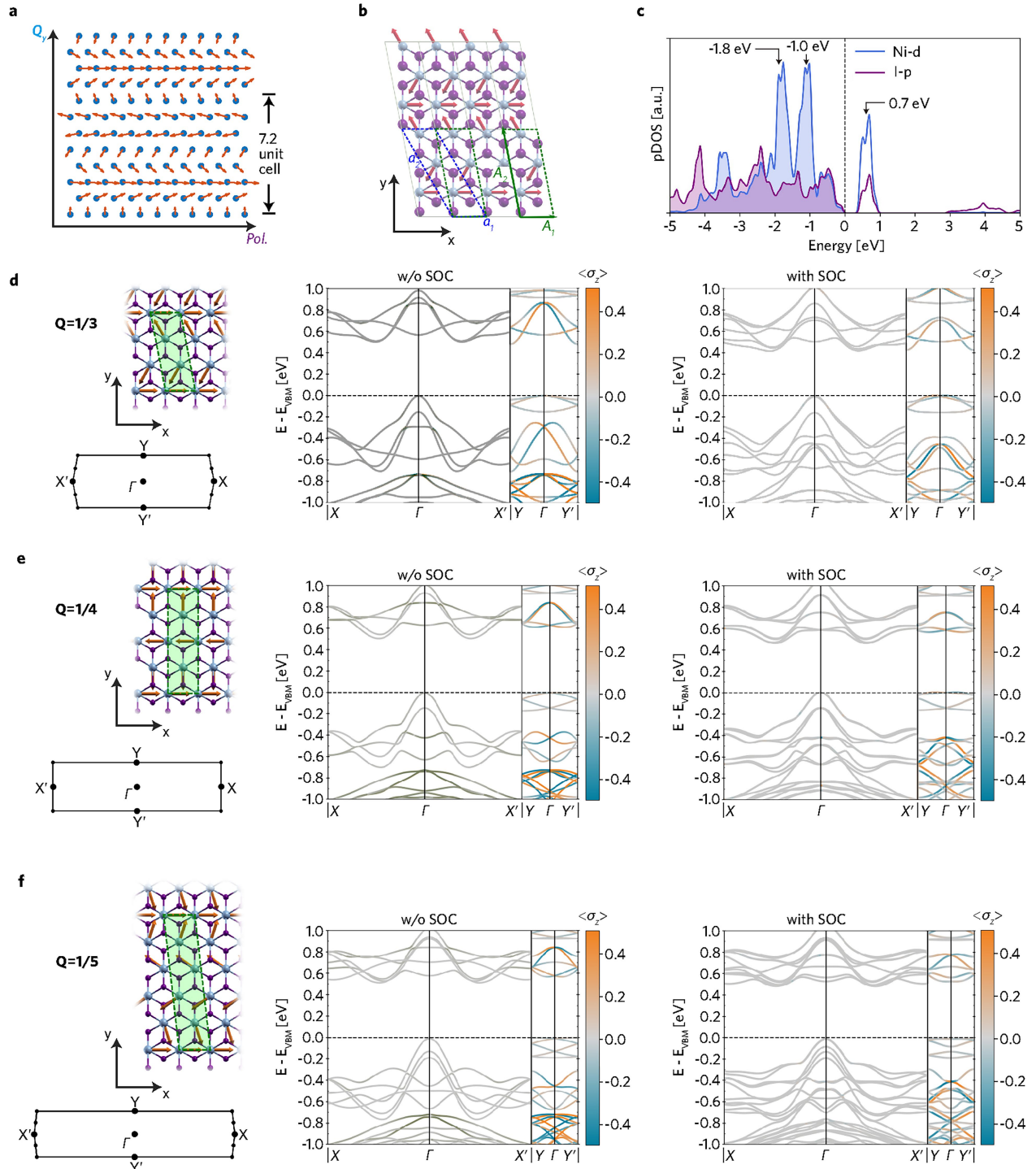
Itinerant electrons with opposite momenta $\pm\mathbf{k} \parallel \mathbf{Q}$ experience opposite effective magnetic fields $\pm B_{\text{eff}}$ owing to the Kondo interaction J_{ex} with the localized magnetic moments of the spin helix. When the spin chirality switches, the sign of effective magnetic field also reverses, showing opposite momentum splitting of spin-up and spin-down channels in left chiral (**a**) and right chiral (**b**). See Supplementary Information Section 3 for further details on this model.

The DFT model of cycloidal (**c**) and helical (**d**) components in NiI_2 . The spin polarization is perpendicular to the spin-spiral plane and antisymmetric along the propagation vector. In the absence of SOC, the non-relativistic band structures are identical, with the spin polarization oriented perpendicular to the spin-spiral plane. When SOC is included, relativistic effects on the band structure depend on the orientation of the spin-spiral plane. However, the odd-parity character of the non-relativistic spin polarization is preserved.



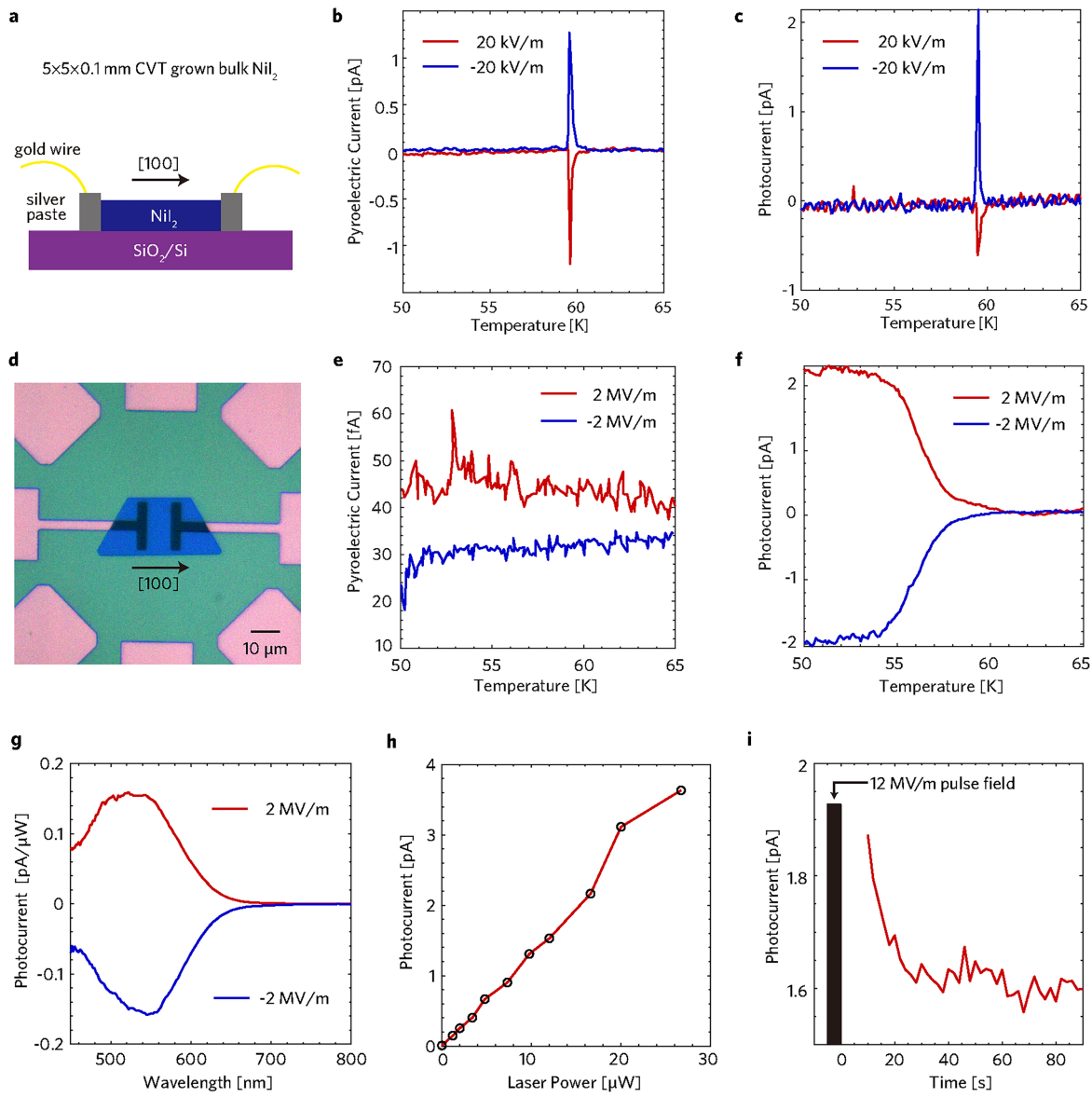
Extended Data Fig. 5 | Comparison of bulk and monolayer spirals.
a, Simulation cell for bulk NiI_2 with a spiral wavevector $\mathbf{Q} = (1/3, 0, 3/2)$, symmetry-wise compatible with the experimentally reported propagation vector but with a different pitch, highlighting the relationship with the computational model used for a single layer, alongside the corresponding Brillouin zone **b**. $X, X', Y, Y', \Gamma (\bar{X}, \bar{X}', \bar{Y}, \bar{Y}', Z)$ are the high-symmetry points in the $k_z = 0$ ($k_z = 1/2$) plane at the boundary of the first Brillouin zone. Because the

band structure is insensitive to the spiral plane in the absence of SOC, without loss of generality, we have considered spins rotating in the x - y plane, realizing a pure cycloidal component in the monolayer case. The monolayer non-relativistic band structure (**c**) is compared with the bulk one in the $k_z = 0$ (**d**) and $k_z = 1/2$ (**e**) planes, confirming the weak interlayer interactions and substantial vdW character of bulk NiI_2 , as well as the same spin-polarization effect along the direction perpendicular to the spiral plane.



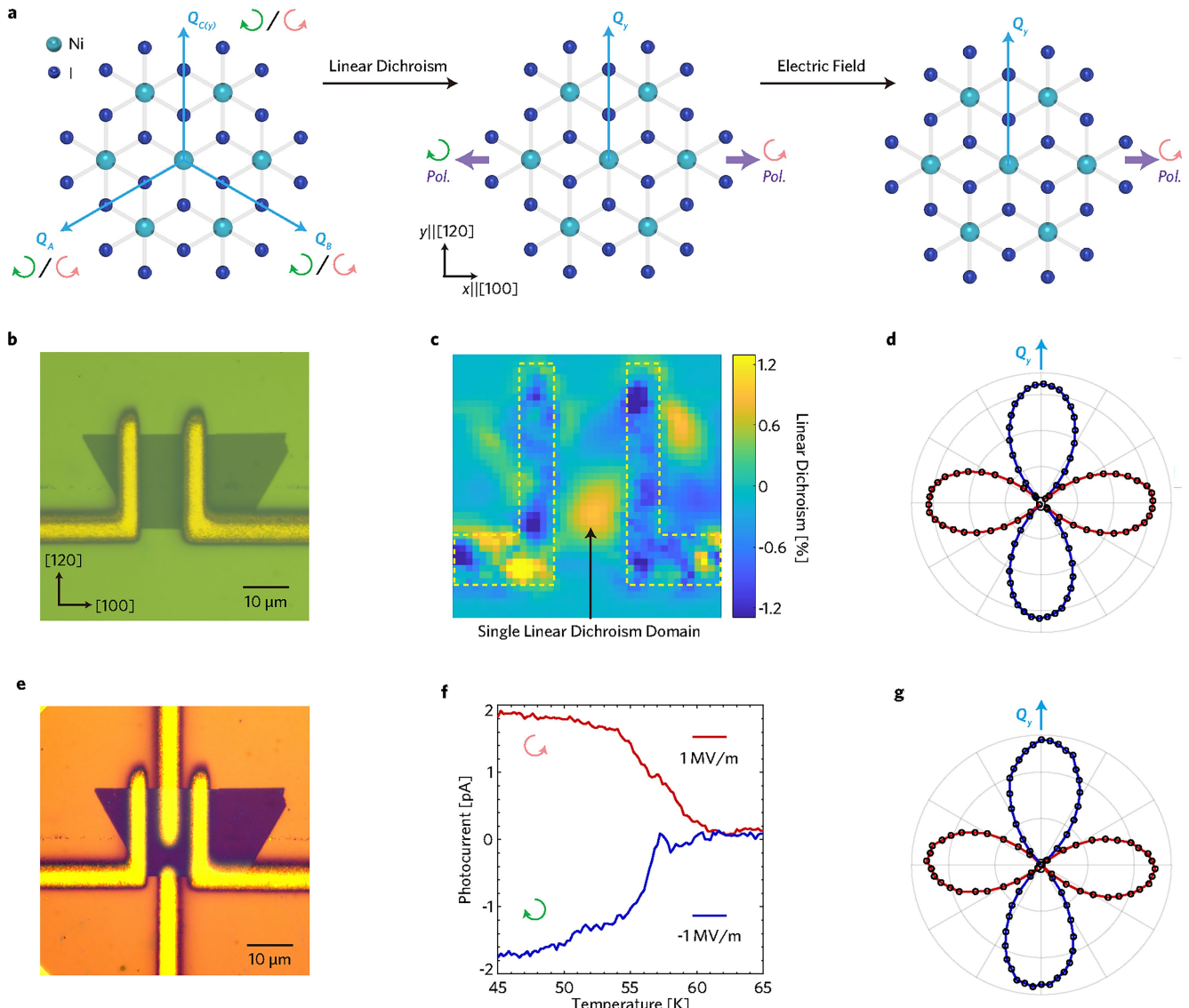
Extended Data Fig. 6 | DFT model of spin helix with propagation vector $Q=1/n$ (n is period). **a.**, In-plane projection of spin helix in NiI_2 is a cycloid propagating along $Q_y \parallel [120]$, inducing ferroelectric polarization along $\text{Pol.} \parallel [100]$. **b.**, The DFT model of spin helix in NiI_2 was simplified as a cycloidal-type spin spiral propagating along $y \parallel [120]$, with spin spiral in the x - y plane perpendicular to $z \parallel [001]$, inducing ferroelectric polarization along $x \parallel [100]$. The period of the spin spiral for DFT calculation was three Ni spin ($n = 3$), unless specified. The Wigner-Seitz cell (the green cell) was used for DFT calculation,

as its reciprocal cell represents the first Brillouin zone. **c.**, Projected density of states of NiI_2 in the spin-spiral phase. The most pronounced Ni-3d characters are at $E = E_{\text{VBM}} - 1.8, -1.0$ and $+0.7 \text{ eV}$. DFT model of spin helix in NiI_2 with period $n = 3$ (**d**), $n = 4$ (**e**) and $n = 5$ (**f**). Magnetic supercells used to model the spin helices are presented, together with their first Brillouin zones. The $\langle \sigma_z \rangle$ spin polarization is quantitatively influenced by periodicity and SOC, yet the odd-parity nature remains robust irrespective of them.



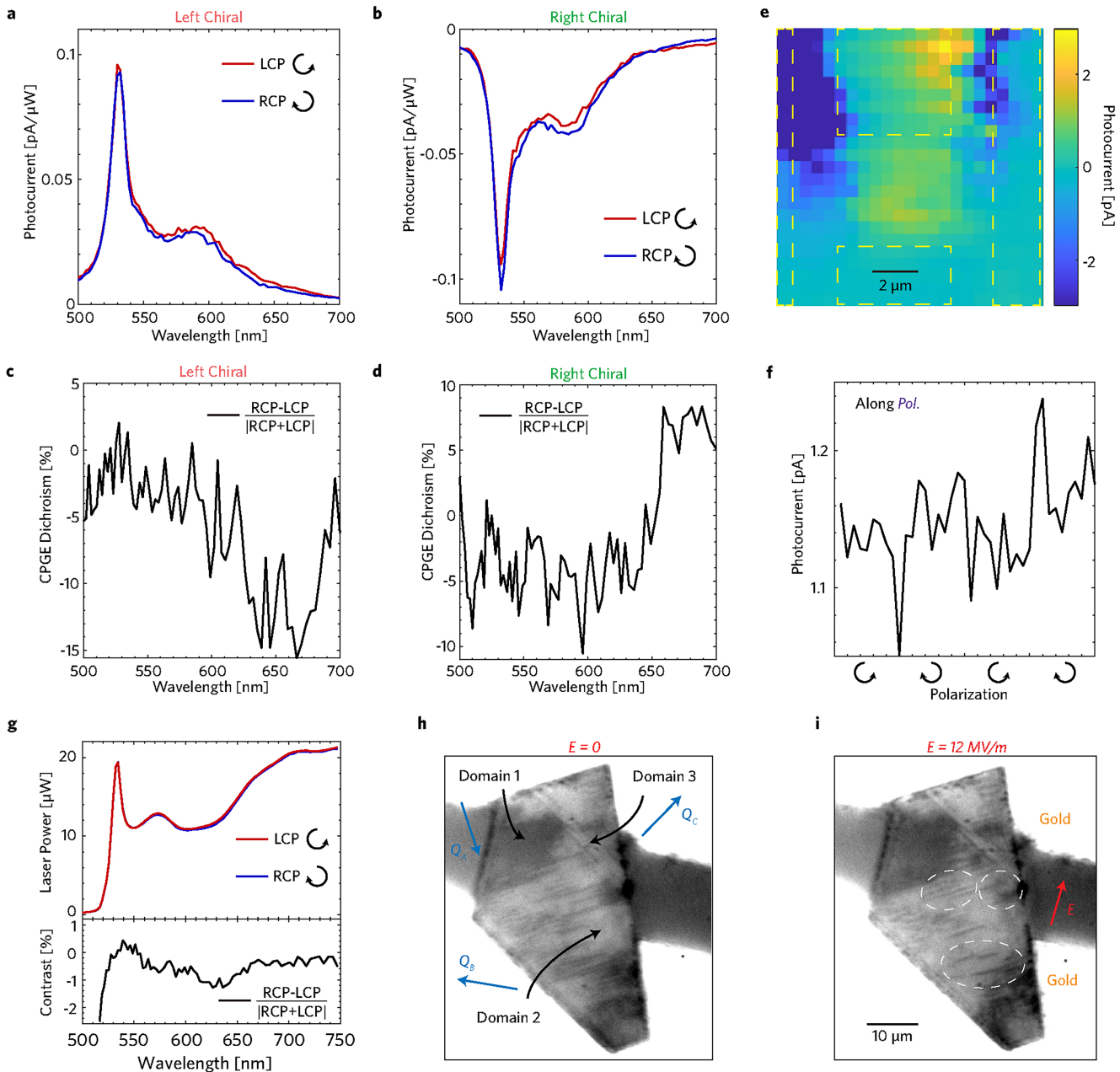
Extended Data Fig. 7 | Comparison of pyroelectric current and zero-bias photocurrent measurements. **a**, Schematic of the CVT-grown bulk NiI_2 device. Electric field is applied along the crystallographic [100] direction. **b**, Pyroelectric current of the device in **a**. **c**, Zero-bias photocurrent of the device in **a**. There is no clear photocurrent below the transition temperature and the current is dominated by the pyroelectric current. The absolute value of pyroelectric current under illumination is not reliable. **d**, Optical image of a 20-nm-thick PVD-grown NiI_2 device. **e**, Pyroelectric current of the device in **d**. The pyroelectric current in a 20-nm-thick flake is expected to be below the attoampere level and there is no clear signature of multiferroic transition at

the femtoampere level in the temperature-dependent measurements. **f**, Temperature-dependent zero-bias photocurrent of the device in **d** shows clear transition near 59.5 K. **g**, Spectra of zero-bias photocurrent after opposite field cooling. **h**, Zero-bias photocurrent shows linear dependence with the laser power at 532-nm illumination. **i**, Stabilization time of zero-bias photocurrent after applying a 12 MV m^{-1} pulsed electric field to switch the ferroelectric polarization. The current stabilized at around 40 s after the pulsed electric field. The laser was focused using a $20\times$ objective to form a 5- μm -diameter illumination at the centre of the NiI_2 flake for the bulk photovoltaic effect measurement.



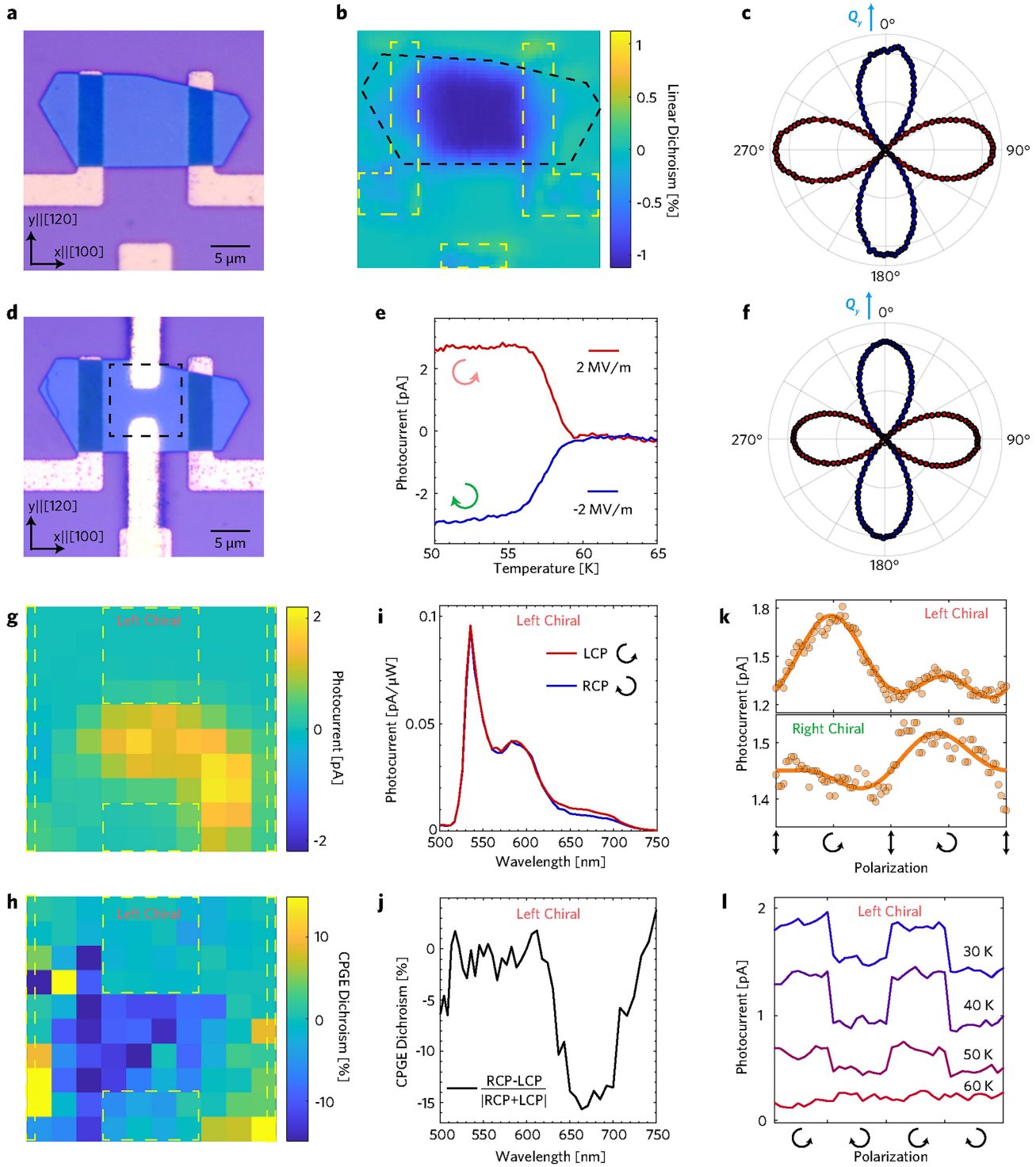
Extended Data Fig. 8 | Device fabrication for the CPGE measurement in NiI_2 . **a**, Schematics of a single-domain selection procedure. In total, there are six multiferroic domains, with propagation vectors denoted as \mathbf{Q}_A , \mathbf{Q}_B and \mathbf{Q}_C . Linear dichroism can distinguish the propagation direction, selecting a pair of chiral domains with opposite ferroelectric polarization (Pol.) perpendicular to the propagation vector (\mathbf{Q}_C domain is denoted as \mathbf{Q}_y). Applying electric field further selects a single spin helix domain. **b**, Optical image of a NiI_2 flake with one pair of gold electrodes transferred along the [100] direction. **c**, Linear dichroism scanning with light linearly polarized along the [120] direction at 30 K. The dashed yellow lines mark the position of the gold electrodes. The state was

prepared by 1 MV m^{-1} field cooling. **d**, Angular-dependent linear dichroism at the single linear dichroism domain region marked in **c**. **e**, Another pair of gold electrodes were transferred along the [120] direction at the single domain region. **f**, Temperature-dependent zero-bias photocurrent along the [100] direction shows the switching of ferroelectric polarization in the CPGE device after $\pm 1 \text{ MV m}^{-1}$ field cooling. **g**, Angular-dependent linear dichroism at the single domain region after transferring the gold electrodes at 30 K. Linear dichroism domain distributions are not sensitive to external electric field and they have memory between different cooldowns.



Extended Data Fig. 9 | CPGE spectra and imaging at 30 K. Left and right circularly polarized photocurrent spectra along \mathbf{Q}_y after 1 MV m^{-1} (**a,c**) and -1 MV m^{-1} (**b,d**) field cooling along the ferroelectric polarization direction. The CPGE dichroism shows strongest contrast near 680 nm. **e**, Photocurrent along \mathbf{Q}_y scanned at the sample region. The yellow squares mark the position of the gold electrodes. The sample region between the gold electrodes shows non-vanishing photocurrent. The laser was focused using a $50\times$ objective and the spot size is around $2 \mu\text{m}$. **f**, When the polarization of incident light was toggled between LCP and RCP, the photocurrent along ferroelectric polarization did not show a clear difference. **g**, Wavelength-dependent measurement of the laser power for both LCP and RCP at the sample position. Our optical set-up

introduces a 0.4% artefact difference between LCP and RCP at 680 nm, which is much smaller than the CPGE observed in the experiment. **h**, Wide-field cross-polarized imaging for a 100-nm-thick sample at zero-field cooling at 30 K. Some stripe-like domains are narrow with width less than 0.5 microns. **i**, Cross-polarized imaging of the same sample at 30 K with 12 MV m^{-1} field cooling. Overall, the domain distribution remains largely unchanged (memory effect), both between and on the electrodes. Some domains exhibit changes between temperature cycles, as indicated by the white circles. However, CPGE is still a robust probe of odd-parity spin polarization (Supplementary Information Section 5).



Extended Data Fig. 10 | Second CPGE device. **a**, Optical image of the second CPGE device. **b**, Linear dichroism (LD) imaging at 30 K shows a large single LD domain region between electrodes. **c**, Angular-dependent LD at 30 K shows that the single LD domain has propagation vector \mathbf{Q}_y along the [120] direction. **d**, Optical image after transferring one more pair of electrodes along the \mathbf{Q}_y direction. The square marks the region in which the photocurrent scanning was done in **g** and **h**. **e**, Field cooling along Pol. shows switching of ferroelectric polarization. **f**, Angular-dependent LD at 30 K between the top and bottom electrodes in **d** shows that the LD domain has memory. **g**, Photocurrent (left circularly polarized 680-nm photoexcitation) along \mathbf{Q}_y scanned at the sample

region at 30 K. **h**, The CPGE scanning with 680-nm photoexcitation shows that the main contribution of CPGE is from the Ni_2 sample. The CPGE between the left and bottom electrodes is because of the weak photocurrent at this region, which results in higher noise of CPGE. The laser was focused using a $50\times$ objective forming a 2- μm spot size and each pixel of the mapping is 1 μm . **i**, Photocurrent spectra at 30 K shows a clear splitting between LCP and RCP at 630–720 nm, in which the CPGE dichroism reaches -15% , as shown in **j**. **k**, Angular dependence at 30 K and temperature dependence (**l**) of CPGE with 680-nm photoexcitation. The change of CPGE coefficient for right chiral is probably because of domain redistribution in thermal cycles.

Article

Extended Data Table 1 | Fitting parameters of the photogalvanic effect in NiI_2

Parameters	C	L_1	L_2	D
Left Chiral	0.0966	0.0147	-0.1418	1.3995
Right Chiral	-0.1085	-0.1362	-0.0745	-1.4790
Along Pol.	0.0068	0.1684	-0.0022	1.2540

C is the CPGE coefficient, L_1 and L_2 are the LPGE coefficients and the constant D contains other effects, such as photovoltaic effect at the contacts, Dember effect and photon drag effects.

CPGE is a spin-dependent intrinsic effect, whereas LPGE has both intrinsic and extrinsic contributions.